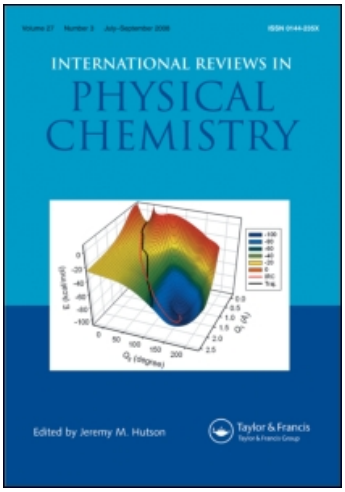

International Reviews in Physical Chemistry
Publication details, including instructions for authors and subscription information:
http://www.informaworld.com/smpp/title~content=t713724383

Molecular vibrational energy flow: Beyond the Golden Rule

M. Gruebele; R. Bigwood

Online publication date: 26 November 2010

To cite this Article Gruebele, M. and Bigwood, R.(1998) 'Molecular vibrational energy flow: Beyond the Golden Rule', International Reviews in Physical Chemistry, 17: 2, 91 — 145
To link to this Article: DOI: 10.1080/014423598230117
URL: http://dx.doi.org/10.1080/014423598230117

INTERNATIONAL REVIEWS IN PHYSICAL CHEMISTRY, 1998, VOL. 17, NO. 2, 91–145

Molecular vibrational energy flow: beyond the Golden Rule

by M. GRUEBELE and R. BIGWOOD

Department of Chemistry and Beckman Institute for Advanced Science and Technology, University of Illinois, Urbana, IL 61801, USA

This article reviews some recent work in molecular vibrational energy flow (IVR), with emphasis on our own computational and experimental studies. We consider the problem in various representations, and use these to develop a family of simple models which combine specific molecular properties (e.g. size, vibrational frequencies) with statistical properties of the potential energy surface and wavefunctions. This marriage of molecular detail and statistical simplification captures trends of IVR mechanisms and survival probabilities beyond the abilities of purely statistical models or the computational limitations of full *ab initio* approaches. Of particular interest is IVR in the intermediate time regime, where heavy-atom skeletal modes take over the IVR process from hydrogenic motions even upon X–H bond excitation. Experiments and calculations on prototype heavy-atom systems show that intermediate time IVR differs in many aspects from the early stages of hydrogenic mode IVR. As a result, IVR can be coherently frozen, with potential applications to selective chemistry.

Contents

0144–235X/98 $12.00

1. Definitions and scope

1.1. *Intramolecular vibrational redistribution (IVR)*

Vibrational energy flow plays an important role in the reactivity of molecules both in the gas phase and in condensed media. It often redistributes energy among many degrees of freedom on a timescale faster than the breaking of an activated bond. Conversely, it can govern isomerization or reaction rates by making energy available to molecular modes not initially activated. Efficient vibrational energy redistribution therefore becomes an underlying assumption of statistical reaction rate theories, such as RRKM.

Whether such energy flow is more appropriately termed 'relaxation' or 'redistribution' depends on how the world is partitioned into 'system' and 'bath', and on the size of the bath. If we consider the molecule to be our system, and the solvent to be the bath, then vibrational energy relaxation can take place from molecule to solvent. If our system is a vibrational overtone of a large collision-free molecule, and the other modes form the bath, then likewise energy relaxes out of the excited mode with timescale T_1. If the entire isolated molecule is viewed as the system, vibrational energy is conserved and the changes in mode population represent pure T_2 dephasing. If the molecule is sufficiently large, the overlap

$$P(t) = |\langle \Psi(0) | \Psi(t) \rangle|^2, \tag{1.1}$$

which is the survival probability of an initially prepared nonstationary state $\Psi(0)$, closely approaches zero at long times. In this limit it becomes sensible to speak of

'relaxation' out of an initially excited mode into the entire set of $\mathcal{N} = 3N-6$ vibrational modes, even if $\mathcal{N}$ is finite.

The collision-free dephasing process, usually termed 'intramolecular vibrational redistribution' or IVR for short, concerns us here exclusively. Furthermore, we will restrict ourselves to the rotationless case on the ground state electronic surface of covalently bound molecules, where IVR proceeds purely through vibrational couplings. While necessary for the spectroscopic study of small-molecule IVR, Coriolis couplings are negligible in large organic molecules because they scale as

$$E_{\mathrm{Cor}} \approx \hbar/t_{\mathrm{Cor}} \approx \zeta(kT_{\mathrm{rot}}\, B)^{1/2}, \tag{1.2}$$

where ζ is a Coriolis parameter near unity, and $B < 0.1\ \mathrm{cm}^{-1}$ is the average rotational constant. A time even longer than the transitional timescale of interest here (5–100 ps, section 7) must therefore elapse before Coriolis effects contribute to dephasing in large molecules. Internal rotor motions (e.g. methyl groups) are always important and cannot be excluded in any limit (Perry *et al.* 1995).

1.2. *Bright state and eigenstate bases*

The concepts of 'bright states' and 'eigenstates' will be important in the discussion. If an eigenstate Ψ_α of the vibrational Hamiltonian is excited, no dephasing occurs†. However, molecular spectra are rarely a forest of random intensity transitions to eigenstates. They are grouped into features (figure 1.1) (Nesbitt and Field 1996). Excitation of a single feature $\Psi(t)$ with a short coherent laser pulse of (approximately) constant amplitude and phase across a feature creates a state $\Psi(t=0)$ which subsequently evolves as

$$\Psi(t) = \sum_\alpha I_\alpha^{1/2} \exp[-\mathrm{i}\omega_\alpha t]\psi_\alpha \tag{1.3}$$

once the laser is turned off at $t = 0$. I_α are the normalized intensities of the eigenstates accessed from an initial state ψ_0, and ω_α are their angular frequencies ($= E_\alpha/\hbar$). The factors $I_\alpha^{1/2}$ are simply the in-phase amplitudes of each eigenstate created by a constant amplitude and phase laser pulse at $t = 0$. A single feature $\Psi(t)$ can contain one, or a very large number, of eigenstates Ψ_α, depending on the energy and state density (figure 1.1).

The evolved feature $\Psi(t \to \infty)$ has a very complex nodal structure, similar to that of the eigenstates of the anharmonic Hamiltonian at high energy or density of states. In stark contrast, the initial feature $\Psi(t=0)$ generally has a very simple nodal structure which can be characterized by one or a few bright states that carry all the oscillator strength. In the simplest case of one bright state per feature,

$$\Psi(t=0) = \Psi_{\mathrm{bright}} = \sum_{\alpha=1}^{m} I_\alpha^{1/2}\, \Psi_\alpha, \tag{1.4}$$

where Ψ_{bright} is the bright state, taken to be time-independent in our discussion. In

† We will not discuss the following effects: transit-time broadening or spontaneous emission, which can in principle be suppressed by appropriate experimental geometries (e.g. slit-jets or antiresonant cavities); vibronic couplings (more than one electronic state) and the resulting multiexponential processes; the cosine roll-off of $P(t)$ at $t \approx 0$ due to the finite number of eigenstates accessed by the laser pulse; differences between 'relaxed' and 'unrelaxed' emission, all of which are by now well understood (Freed and Nitzan 1980, Fleming 1986, Uzer 1992).

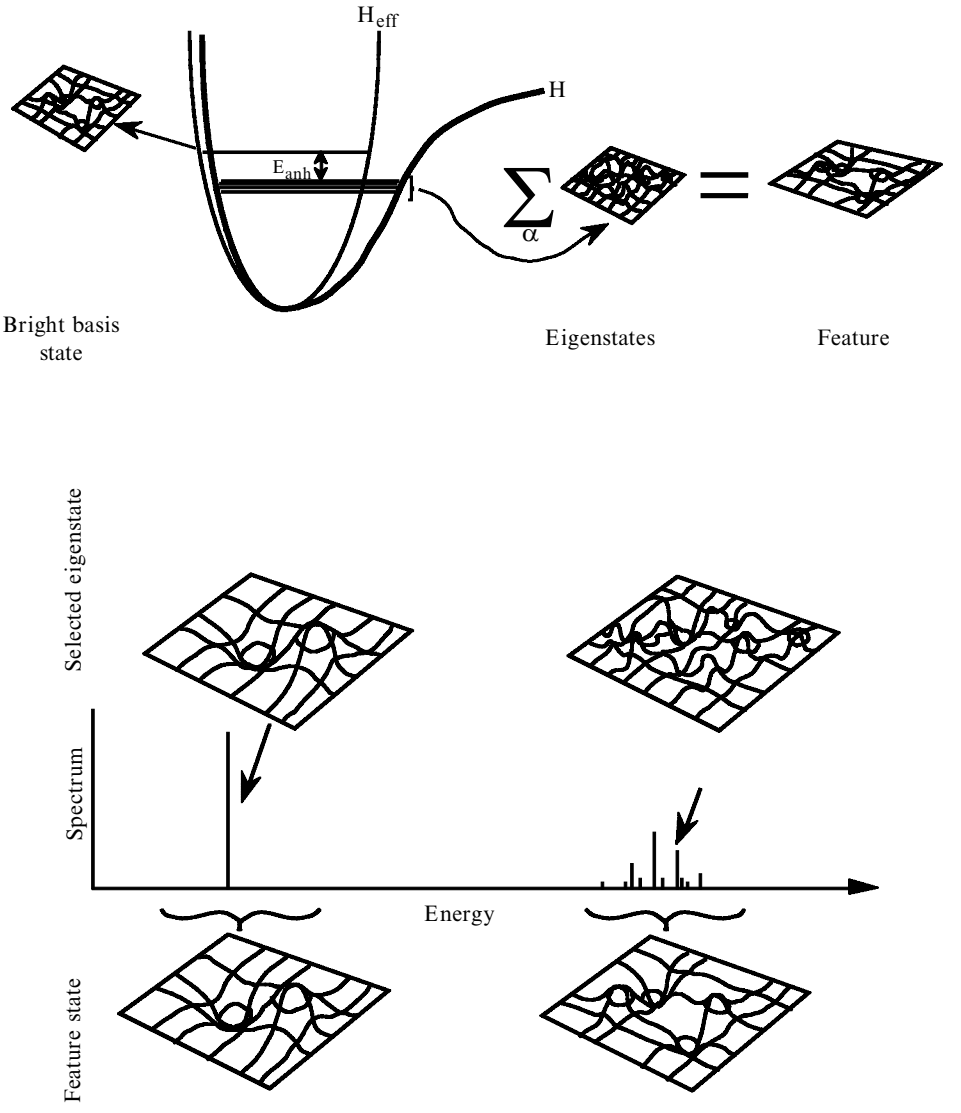

Figure 1.1. Upper diagram: the anharmonic terms in the Hamiltonian lower the feature energy and distort its appearance from that of a bright basis state, but memory of the bright basis state is retained. Lower diagram: an unfragmented and an IVR fragmented spectral feature. The unfragmented feature (low energy) has an eigenstate with a simple normal or local mode structure; the fragmented feature (high energy) consists of eigenstates with a complex structure, even though the wavefunction corresponding to the feature is still relatively simple and best represented in a bright basis.

effect, the anharmonicity of the underlying Hamiltonian has redistributed the oscillator strength from a single bright state over a large number of eigenstates which lie under the envelope of a feature. It is our contention that the bright states in equation (1.4) have certain well defined universal nodal properties resulting from the 'weak' anharmonicity of H, and that these properties are as characteristic of the total Hamiltonian as the complex nodal structure of the eigenstates (figure 1.1; sections 3 and 4).

It is often discussed in the literature that bright states are arbitrary because they depend on the manner of excitation, and that $P(t)$ has no meaning unless the manner of excitation is precisely specified. This view results from concentrating on the early timescales of IVR (say, $P(t) > 0.1$), rather than what we term the transitional or late timescales, which form the bulk of our discussion. This view is correct from a practical point of view at short times, where specific couplings dominate the dynamics. It is also correct *in principio* on any timescale, if infinite predictive accuracy is demanded. However, it is more useful in many cases to concentrate on the universal properties of bright states, rather than on their 'zoology'. The entire problem of IVR is, after all, simply the question of how experimentally prepared features (initially assemblages of a few bright states) evolve in time into a phase-decorrelated set of eigenstates.

Phase decorrelation is the key: bright states Ψ_{bright} are not eigenstates of the total vibrational Hamiltonian H, but they are highly phase correlated. The nodal structure of $\Psi_{\text{bright}} = \Psi(t = 0)$ is universally simpler than that of the constituent eigenstates Ψ_α (Davis 1993), unlike the nodal structure of a time-evolved highly fragmented feature $\Psi(t \to \infty)$. The bright states and the eigenstates lie at opposite extremes of a dynamical hierarchy (Davis 1995).

This is not an accident, but a direct result of underlying properties of the vibrational Hamiltonian (section 4). Briefly, the reasons are: (1) the anharmonic energy becomes comparable to the harmonic contribution only near the dissociation limit D and D is much larger than the vibrational spacing ω due to the small value of the Born–Oppenheimer parameter $a = (m_e/m_{\text{nuclear}})^{1/4} \approx 0.1$; (2) the virial or Hellman–Feynmann principle asserts that any kinetic/potential partitioning is arbitrary and coordinate-dependent, and does not affect the scaling law of anharmonic couplings (e.g. local and normal mode couplings scale the same). These two points will be discussed in more detail in section 4 (Madsen *et al.* 1997). The scaling of anharmonic couplings is a universal property of H, just as is the trivial absence of couplings in the eigenstate basis of H. Bright states are remnants of the $a \to 0$ limit of the vibrational Hamiltonian.

The simple structure of bright states accounts for the success of what we will label 'bright state bases', such as the normal mode, diagonal anharmonic normal mode, and local mode pictures. These are eigenbases $\{\Psi_i\}$ of quadratic or slightly corrected quadratic zero-order Hamiltonians of the type

$$H_0 = \sum_{i,j=1}^{\mathcal{N}} g_{ij}\, \eta_i\, \eta_j, \tag{1.5}$$

where $\{\eta_i\}$ is a set of $2\mathcal{N}$ conjugate momenta and coordinates (e.g. Cartesian, or Morse-based in the diagonal anharmonic picture). At low energies, the resulting zero-order states are a good representation of the eigenstates of H, which are simultaneously the bright states (figure 1.1). 'Good' means that only one or a combination of a few basis functions provide an excellent description of the low-energy eigenstates. At high energies, they are no longer a good representation of eigenstates, but still a good representation of unrelaxed features $\Psi(t = 0)$ of H and can be constructed from eigenstates at least approximately using equation (1.4).

Note that in this article we will not argue in favour of any specific bright basis such as normal modes versus local modes: a certain feature $\Psi(t = 0)$ may require three normal mode basis functions versus only one local mode basis function to be well represented, but these differences are insignificant compared to the tens or thousands of eigenstates that might be needed to represent a highly fragmented feature state at

high energy and density of states. This was already recognized by Freed about 20 years ago in terms of 'intermediate' and 'statistical' limits, albeit without justification in terms of the Born–Oppenheimer parameter and virial principle (Freed 1976a, b).

Of course most vibrational wavefunctions in a bright state basis are not *experimentally* bright states. While all bright state basis functions are distinguished by an easily assignable nodal structure, only a few states have significant transition dipole moments in any given experimental configuration. For pure vibrational transitions, these are usually overtone or simple combination states; for vibronic transitions, they are transitions involving appropriate quantum number changes in Franck–Condon active modes. Once a consistent basis has been picked, the mechanism of IVR can be understood in terms of that basis. We argue that a purely bright state basis is the most useful one (sections 3 and 4) both for gaining insights into IVR and from a computational point of view.

Hamiltonians such as equation (1.5) generate a bright basis because they can be transformed into smoothed effective Hamiltonians of the type

$$H_{\text{eff}} = \sum \omega_i (v_i + \tfrac{1}{2}) + \sum \chi_{ij} (v_i + \tfrac{1}{2})(v_j + \tfrac{1}{2}) + \cdots \tag{1.6}$$

where ω_i and χ_{ij} are 'predictable' parameters. In such an action representation (section 3.2.), the full Hamiltonian H would become a resonance Hamiltonian with additional ladder terms of the type $c_{nm}\, a\dagger^n a^m$, where the c_{nm} would be increasingly 'unpredictable' due to accidental resonances at higher energy or density of states.

The basis functions Ψ_i of equations (1.5) and (1.6) are not identical to the unrelaxed experimental features $\Psi(t = 0)$ of equation (1.4); yet at high energy or state density, they are much closer to the experimentally defined bright states than to the eigenstates, which have a complicated nodal structure due to $c_{nm}\, a\dagger^n a^m$ resonant terms. Unrelaxed features and bright basis states can be nearly overlapped by simple transformations of the type

$$\Psi(t = 0) \approx RS\Psi_i \tag{1.7}$$

where S is a linear scaling transformation $q_i \rightarrow cq_i$, and R is a rotation operator (figure 1.1). For example, a nominally assigned $v_{\text{CH}} = 6$ spectral feature, even in the absence of extensive IVR fragmentation, would require $v_{\text{CH}} = 4, 5, 6, 7$ and a few other normal mode basis functions to represent the centre energy of the transition accurately. Even fewer basis functions would be required in a diagonal anharmonic mode basis. However, a single 'stretched' normal mode wavefunction $S\Psi_i(v_{\text{CH}} = 6)$, suffices to accurately represent the nominally $v_{\text{CH}} = 6$ spectral feature.

In the presence of multiple resonances, all bright state bases are roughly 'equally bad' representations of eigenstates because parameters such as χ_{ij} share the same fundamental scaling as less predictable specific resonance terms c_{nm} (Madsen *et al.* 1997) (section 4). At short times, such a basis can be compared decisively with experiments *only* if accurate matrix elements of the full vibrational Hamiltonian H can be calculated. Yet $P(t)$ at short times obviously does not provide a complete picture of IVR, especially if only one class of bright states is investigated (e.g. X–H stretching features). At longer times, the complexity of the wavefunction evolves from a simple nodal structure to a complex structure (Davis 1993, Wu 1995). This structural hierarchy is governed by the anharmonicity of the underlying Hamiltonian, and the resulting $P(t)$ shows evidence of universal features such as power law decays (Schofield and Wolynes 1993, Gruebele 1996c), many of which cannot be predicted using purely statistical assumptions (see sections 6 and 7).

1.3. *Application of statistics*

Statistical descriptions of a system can be of two types. They can be maximally decorrelated (or 'random') in their class, such as the Gaussian orthogonal ensemble (GOE) (Brody *et al.* 1981), or they can retain residual correlations of the system parameters.

If molecules of large size or at high energy were always in the 'maximally random' statistical limit, statistical pictures such as the Golden Rule could fully describe the 'kinetics' of IVR (Freed and Gelbart 1971). However, they fail to do so because bright states and features are coupled by terms of the order of $E_{\text{elec}}\, a^n$, where E_{elec} is the electronic energy scale (~ 2 eV), and n is the difference in the node number of two bright states (section 3). These couplings can be quite large compared to the *local* density of coupled states, thus violating the assumption of perturbation theory when energy flow is considered from the point of view of features. The Golden Rule actually assumes a mixed bright/eigenstate representation, with uncorrelated couplings from the bright state to the eigenstates, an assumption which is not justified (section 3). The majority of molecules, (small ones at high energies $\gg \omega_i$ and large ones at low energies $\approx \omega_i$) do not behave according to uncorrelated statistics on certain timescales. As one of several consequences, $P(t)$ decays highly non-exponentially at transitional to long times (section 6).

Another reason for looking at bright state bases is our interest in how generic features of IVR (such as initial rate, or long-term survival probability) are affected by specific molecular properties (such as the number of modes, vibrational frequencies, and scaling of higher order vibrational couplings). In larger molecules with at least $N > 3$ second or higher row atoms, basis states are connected by many low- and high-order couplings, and specific resonances are averaged. The universal scaling of couplings then dominates considerations, allowing the use of *some* statistical considerations. Only some statistics can be applied because molecule-specific properties of the vibrational Hamiltonian can still contribute to the dynamics. A judicious choice must be made in the range between purely statistical models such as the GOE and full *ab initio* approaches, which are so far intractable for large quantum systems.

The fact that statistical approaches are fruitful is not to say that IVR is structureless even at intermediate to long times, as assumed in the simplest models. It is already clear that IVR at early times often depends on specific coupling structures (Jortner and Berry 1968, Felker and Zewail 1985). This is the root for the success of studies employing small model systems. It turns out that energy flow between vibrational modes involving heavy atoms shows localization effects even at long times, leading to properties which deviate in some cases from past expectations, and which can explain previously not fully understood experimental results. The localized nature of IVR, which emerges naturally in bright state bases, will be discussed at several points in this review, and ultimately leads to the possibility of controlling and halting the IVR process itself (Gruebele and Bigwood 1996).

1.4. *Timescales*

The fact that features resemble bright states at early times, and eigenstates long after excitation, suggests that IVR must be characterized by at least two timescales, connected by a transitional timescale. Unlike much earlier work, our interest focuses on the transitional and late time periods.

This is illustrated in figure 1.2. At very early times, any set of eigenstates evolving

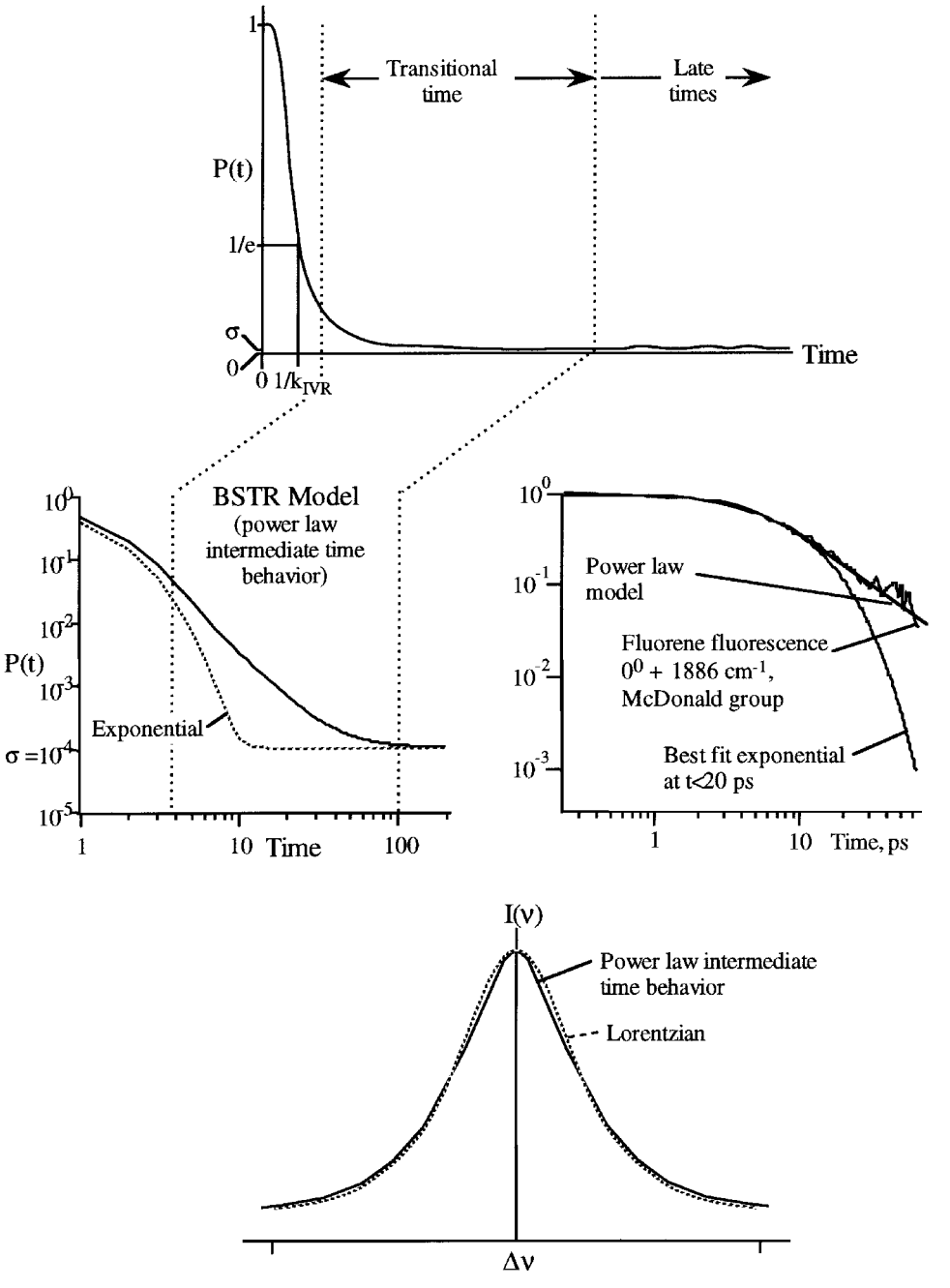

Figure 1.2. Upper diagram: important timescales in IVR. The early timescale where IVR is well described by a '$1/e$ decay' rate k_{IVR} is shown by dashes. It is a well-defined exponential rate in certain cases. The transitional time lies roughly between $P(t) \approx 0.1$, and when $P(t)$ becomes equal to σ on average. This is where quantum beats occur in the 'sparse limit', and novel behaviour, such as power law decay, occurs in the 'statistical limit'. At late times, the IVR wavepacket covers its available phase space, which can be far less than the total available in principle under the spectral envelope ($\sigma > \sigma_{min}$, $F < 1/3$). Middle diagram: log–log representation of the same timescales. Power law behaviour at intermediate time greatly reduces the effective IVR rate. Also shown is

according to equation (1.3) has a cosine roll-off followed by further decay. We characterize the early time by a generalization of the rate often used by experimentalists, which is

$$k_{\mathrm{IVR}} \equiv 1/\tau_{\mathrm{e}} \tag{1.8}$$

where τ_{e} is the time required for $P(t)$ to decrease to $1/\mathrm{e}$. In the case of an exponential decay, k_{IVR} is just the exponential rate constant. For cases where no decay below $1/\mathrm{e}$ occurs (e.g. weak resonance, dominated by quantum beats (Jortner and Berry 1968, Felker and Zewail 1985)), the IVR threshold has not been reached and a rate cannot be defined, although there is some energy redistribution among bright basis states.

If $N = 1/\sigma$ eigenstates with intensities I_α contribute to a feature envelope (e.g. the ten states in fig. 1.1), $P(t)$ of the entire feature cannot decay below an average value of σ (Smith and McDonald 1992) at long times. This is so because with uncorrelated phases, the factors in equation (1.3) still add up to $1/N = \sigma$. A statistical interpretation is that the bright state is distributed over N eigenstates, and $\Psi(t \to \infty)$ retains a fractional bright state character of $\sigma = 1/N$.

If the spectral intensities are known, as in figure 1.1, σ can be readily calculated using

$$\sigma = \sum_{\alpha=1}^{N} I_\alpha^2, \tag{1.9}$$

assuming that the overall intensity of the feature ΣI_α has been normalized (Stewart and McDonald 1983). σ clearly always falls in the range between zero (infinite density of states) and one (no IVR). A closely related quantity is Heller's F parameter (Stechel and Heller 1984) which can be defined as

$$F = \sigma_{\mathrm{min}}/\sigma, \tag{1.10}$$

where σ_{min} is the dilution factor if all eigenstates under the feature envelope were to contribute with maximum intensity while preserving the rate k_{IVR}. Due to quantum mechanical phase cancellation effects, F cannot exceed $1/3$ if the matrix elements of H are real-valued.

The transitional region connecting these two limits is important. Even for large molecules where quantum beats are not an issue, this region nonetheless rarely corresponds to the generally assumed exponential decay. Instead, it shows power law behaviour before leveling off to σ (sections 6 and 7). Power law decays are considerably slower than exponential decays, and lead to a distorted lineshape (figure 1.2). The deviation from Lorentzian is small, but the lineshape is clearly narrowed. This seemingly subtle effect has dramatic consequences. The timescale between τ_{e} and $\langle P(t) \rangle = \sigma$ can cover several orders of magnitude, and the same factors that cause nonexponential behaviour can be exploited to control IVR during coherent laser excitation (Gruebele and Bigwood 1996). The fact that IVR in this intermediate regime is slow compared to the initial k_{IVR} can lead to slower-than-expected isomerization (Leitner and Wolynes 1997). It is very important to keep in mind that a rapid drop of $P(t)$ to 0.1 merely indicates that the equivalent of ten states participate at early times; maximum coverage of phase space ($F = 1/3$), if achieved at all, can be considerably slower.

experimental data on fluorene (Kaufmann *et al.* 1989), adjusted for fluorescence and radiationless effects. It clearly supports the notion of power law decays at intermediate times. The transition from exponential to power law occurs when $P(t)$ is already fairly small, and has a subtle, but dynamically very important effect on the lineshape, which is compared with the standard Lorentzian (lower diagram).

Different experimental approaches tend to be more sensitive to measuring either the early dephasing rate k_{IVR}, or the eventual completeness of the IVR process characterized by σ. Both parameters, as well as the expected behaviour in the transitional time period, must be accounted for by a successful treatment of IVR.

2. A snapshot of past and recent developments

A detailed discussion of the hundreds of papers that have appeared on IVR over the years is beyond our scope. However, to put recent developments into context and to assist the reader who needs more detailed accounts, we briefly discuss some earlier reviews and highlights.

Some of the earliest experimental evidence for the need of a more detailed understanding of intramolecular dynamics came in the form of anomalies in the numerous fluorescence spectra of organic molecules accumulated during the 1930's and early 1940's. Kortüm and Finckh (1943) cite several such examples resulting from intramolecular energy randomization of various forms, including IVR.

Another classic example appears in the studies of unimolecular dissociation reactions and free radical recombination reactions during the late 1940's and early 1950's. Rice, Kassel, Ramsberger and Marcus built this into a coherent picture of the role played by rapid randomization of excess vibrational energy in these two complementary reaction classes (Marcus 1952).

By the late 1950's and early 1960's, there was a great deal of discussion of the entire class of intramolecular dynamics (Harris 1963), including nonradiative (vibronic) transitions and IVR (purely vibrational). Although by then numerous experiments had been performed in solids, liquids, and the gas phase, there was a lack of experimental data at pressures low enough to preclude molecular collisions. Consequently, while large strides had been made in the understanding of electronic radiationless transitions (Kasha 1950), a central issue during this time was how radiationless vibronic/vibrational transitions could occur in isolated molecules.

Bixon and Jortner (1968) showed that such transitions were not only possible but necessary, with a set of compelling arguments based on the available experimental data, and a theoretical explanation of the vibronic couplings that mediate energy flow. A key result of this work was the application of Fermi's Golden Rule relating the rate of vibronic transition to the density of states and the coupling strength by the now familiar formula

$$\Gamma = \frac{2\pi}{\hbar}\rho V_{\mathrm{rms}}^2 . \tag{2.1}$$

In fact, this simple yet elegant result together with the prediction of a Lorentzian lineshape would form the basis for discussions of IVR for the following 20 years, starting with the work of Freed (Freed 1976a, Freed and Nitzan 1980) and Rice (Kay and Rice 1973), who were the first to consider topics such as the effects of state preparation on IVR, appropriate basis representations, random matrix master equations, and the possibility of nonexponential behaviour.

Spurred by advances in laser science and new spectroscopic techniques, interest in IVR intensified during the mid and late 1970's. Renewed interest centred mainly around the characteristic rate with which vibrational redistribution occurred. Experimenters used a wide range of techniques to measure IVR rates in many different organic molecules. Among them were chemical timing experiments (Parmenter 1983), in which the pressure of a quenching agent, and therefore the quenching rate, was used

to gate the dynamics at certain times. Chuang *et al.* (1983) applied the now common pump probe technique to this problem.

In addition to determining that IVR rates can range from picoseconds to nanoseconds, several 'anomalies' were seen in these experiments. Parmenter (1983) observed that energy appeared to be transferred preferentially to states with small quantum number differences n, with an empirical scaling factor 10^{-n}. Non-statistical behaviour was observed even at high vibrational energies in glyoxal (Naaman *et al.* 1979), and this work laid the foundation for later quantum beat experiments. The theoretical understanding of IVR progressed hand in hand with the experiments. Rice, Marcus, Stuchebrukhov (1986), and later Heller contributed to these advances with their semiclassical and quantum mechanical models, which are extensively reviewed by Uzer (1991).

During the 1980's, the body of experimental data continued to grow, as did the range of experimental techniques used to study IVR. Many excellent reviews of the work done during this period exist (Smalley 1982, Parmenter 1983, Bondybey 1984). A few of the most notable advances include multiphoton ionization (Smalley 1982), stimulated emission pumping used to study IVR for the first time on the ground state potential surface (Abramson *et al.* 1984), multiphoton dissociation (Stephenson and King 1978), parametric down conversion to achieve picosecond resolution optical gating (Moore *et al.* 1983), resonance fluorescence (Stewart and McDonald 1983), time-resolved fluorescence techniques (Zewail 1983), multiphoton up-pumping (Puttkamer *et al.* 1983), hydrogen attachment for preparing molecules in highly excited vibrational states (Trentwith *et al.* 1982), and time-resolved infrared emission (Stewart and McDonald 1983). During this period the effects of residual coherence in 'intermediate' size systems emerged (Muehlbach and Huber 1986, Felker and Zewail 1985, Puttkamer *et al.* 1983). The range of molecules studied also grew dramatically, and spanned simple systems like acetylene (Abramson *et al.* 1984) that were most amenable to theoretical treatment, to large organic molecules, through which the effects of alkyl chain length (Smalley 1982) and overall molecular size and functional groups (Stewart and McDonald 1983) could be extracted.

As the available experimental database increased, so did the number of apparent exceptions to the rules. A question central to the validity of the RRKM theory of reaction rates is the ultimate degree of randomization. Rice was among the first to discuss the issue of ergodicity in IVR (Nordholm and Rice 1974), followed by Reinhardt's semiclassical quantization treatment (Reinhardt 1982) and Stechel and Heller (1984) in the developing framework of quantum chaos. Several workers questioned the validity of the direct one-step bright state to bath couplings characteristic of the Golden Rule picture, and proposed a sequential 'tier' picture as an improvement. A hierarchical picture of IVR in terms of wavefunctions was introduced by Davis (1995).

The increasing power of computers began to make fully quantum mechanical simulations of small systems feasible (Bullock *et al.* 1990), in addition to classical trajectory simulations and dynamics which started in the 1960's (Bunker 1962) and continue (Ezra *et al.* 1987, Lu and Hase 1988, Martens and Reinhardt 1990). Powerful new numerical methods aimed at solving the time-dependent Schrödinger equation were required to carry out such simulations (Feit *et al.* 1982, Kosloff and Kosloff 1983). Wyatt's recursive residue generation method (RRGM) (Wyatt 1989) represents the most significant step in the direct time-independent treatment of large Hamiltonian matrices.

Non-molecular model systems of coupled oscillators and their properties also attracted significant interest. These range from classical simulations on low-dimensional systems (Founargiotakis *et al.* 1989) to effective resonance Hamiltonians (Kellman and Xiao 1990, Martens 1992) and purely statistical treatments (Persch *et al.* 1988). The body of this work done before 1990 is also the subject of a detailed review (Uzer 1991).

High-resolution spectroscopy, which had been enormously successful in characterizing small molecules at low energies, was pushing the eigenstate limit to higher energies and densities of states in the 1980's, through the use of narrower-bandwidth lasers (McIlroy and Nesbitt 1989) and application of double resonance techniques (Go *et al.* 1993, Lehmann *et al.* 1994) to explore IVR in a range of organic molecules. Available eigenstate resolution data allowed detailed statistical analyses of molecular spectra under the influence of IVR and related couplings (Lehmann 1991, Shalev *et al.* 1992, Georges *et al.* 1995). Advances continued in the area of ultrafast techniques, including the time-resolved emission experiments of Smith and McDonald (1992) and correlated photon counting studies of Zewail (1985).

New theoretical models and simulations appeared during the 1990's that deviated fundamentally from the standard Golden Rule picture. Notably, ideas related to Anderson localization were applied to IVR, yielding a number of unexpected results (Logan and Wolynes 1990). An essential feature of these models is the notion that levels share direct couplings primarily with levels that are nearby in quantum number space, reminiscent of Parmenter's earlier experimental deduction (Parmenter 1983). The detailed nature of level connectivities, or Hamiltonian topology, was shown to have profound effects on IVR, such as a linear rather than quadratic dependence of the decay rate on anharmonic coupling strength. This type of model was complemented in the time domain by scaling analysis, indicating the possibility of power law decays ($t^{-(\mathcal{N}-1)/2}$) (Schofield and Wolynes 1993) rather than exponential rate decays.

The techniques for computing IVR spectra with spectroscopic accuracy continued to improve (Bentley *et al.* 1989, Iung and Leforestier 1992). A tier model was used by Stuchebrukhov *et al.* (1993) to propose and test superexchange (what we term here 'off-resonant') IVR, and the special behaviour of rotor modes was considered in more detail (Martens and Reinhardt 1990, Perry *et al.* 1995).

Our experimental and theoretical work fits into this most recent era. From a theoretical standpoint, we are particularly interested in large-scale simulations to see under what circumstances deviations from the Golden Rule appear in large systems (discounting quantum beats and similar sparsity-related phenomena). The partially statistical, partially molecular detail-based models we have developed are ideally suited for this case (Bigwood and Gruebele 1995b, Gruebele 1996c, Madsen *et al.* 1997). In this connection, the scaling properties of the vibrational Hamiltonian alluded to in section 1 and discussed in section 4 are of great importance. There are qualitative differences between IVR at early and intermediate times (Bigwood and Gruebele 1995b, Gruebele 1996c), and between IVR initiated in hydrogenic modes (off-resonant) and heavy-atom modes (on-resonant) (Bigwood and Gruebele 1995b, 1997). Experimentally we have therefore studied 'heavy-atom' IVR because it more closely mimics the behaviour of large molecules at long times than initiation of energy flow from hydrogenic modes. In experiments, often only one or a few series of $P(t)$ are available. $P(t)$ provides only a small window on the redistribution process, a window that can be shifted by watching energy flow among second and third row atoms (Geers *et al.* 1994, Bigwood *et al.* 1998, Green *et al.* 1998) rather than from XH stretches.

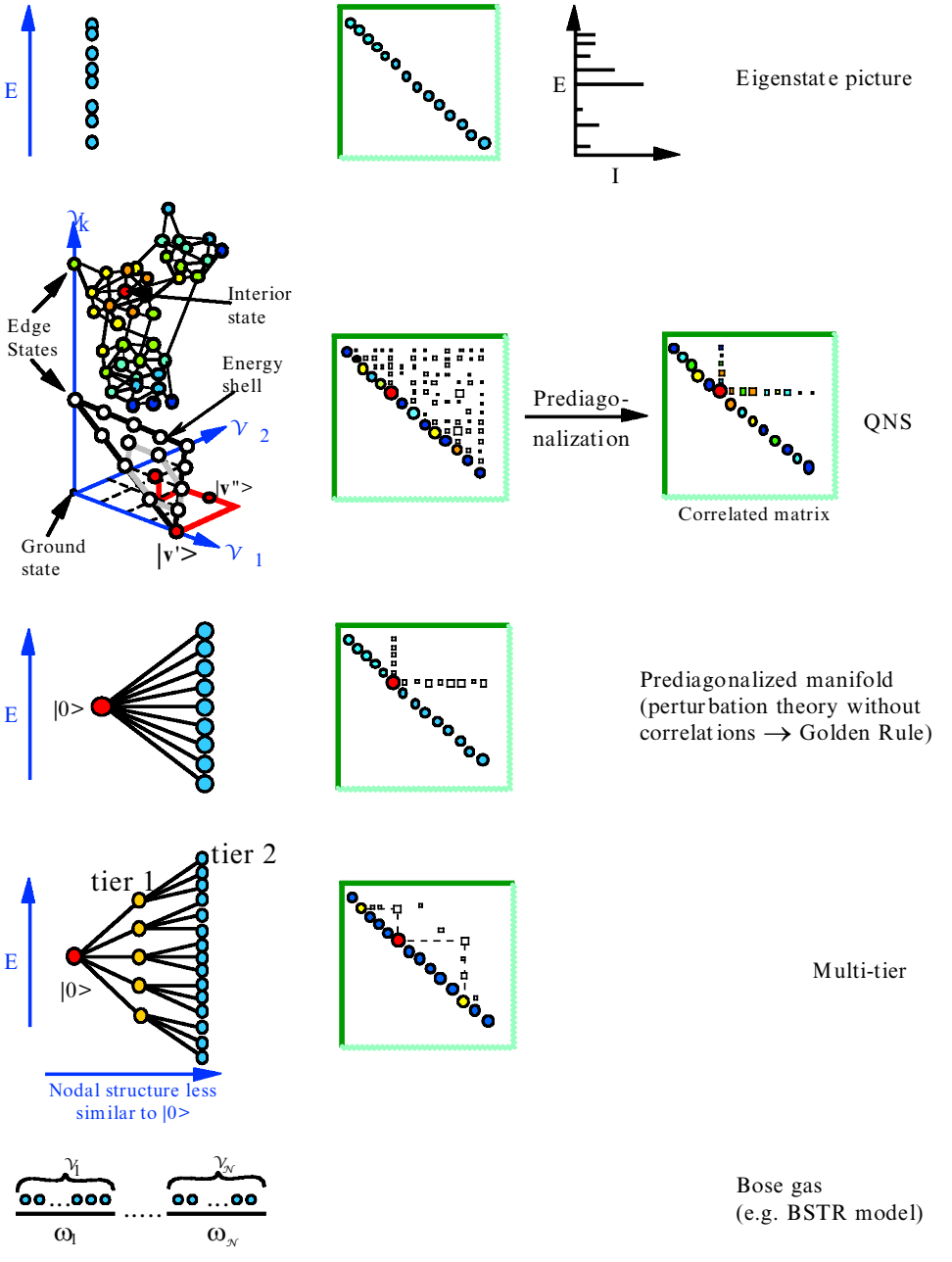

Figure 3.1. Pictorial representations of IVR. From top to bottom the diagrams represent the following. (1) Eigenstate picture; no information about intensities is intrinsic to this picture and they must be provided separately. (2) Quantum number space (QNS) picture; intensities arise from the mixing of an experimentally bright state with other bright basis states. (3) Prediagonalized manifold; intensities arise from coupling a single bright basis state to an eigenstate-like manifold of dark states. If correlations are neglected, the Golden Rule results if the perturbation theory assumptions of large density of states and small rms coupling are not violated. (4) Tier picture; includes no interference from coupling loops in Cayley tree implementation. (5) Bose-gas picture; the $\mathcal{N}$ vibrational modes are considered as receptacles for an arbitrary number of quanta.

A recent theoretical (Leitner and Wolynes 1997) paper closes the RRKM–IVR loop full-circle: it uses a factorized Hamiltonian (Bigwood and Gruebele 1995b, Gruebele 1996c, Madsen *et al.* 1997) to investigate how IVR leads to slower-than-RRKM isomerization of stilbene, a long-standing model system for both theory and experiments.

3. Visualizing IVR

3.1. *Eigenstate picture*

Figure 3.1 shows five pictorial representations of the IVR process. The simplest is the eigenstate picture itself. Each eigenstate has a specific transition dipole moment with the state $|0\rangle$ from which the transitions originate, resulting in a spectral envelope. The spatial structure of the eigenstates can be complicated, and on a state-by-state basis offers little insight into why a particular region of the spectrum shows a simple Lorentzian-like spectral feature, as opposed to a continuous distribution of randomly varying intensities.

3.2. *Quantum number space model*

At the opposite extreme, we consider the bright basis picture, or quantum number space (QNS) picture (figure 3.1). It is important that the basis chosen be a bright basis (section 1), whose states have simple well defined nodal patterns. This could be achieved with a normal mode, local mode, or diagonal anharmonic normal mode Hamiltonian H_0. A closely related phase space representation is very commonplace in the classical dynamics community (Lichtenberg and Lieberman 1983) but is rarely used in quantum mechanical discussions of IVR (Martens 1992). Note that QNS, like action space, has only half the dimensionality ($\mathcal{N}$) of the full phase space ($2\mathcal{N}$), where $\mathcal{N}$ is the number of vibrational degrees of freedom.

Consider two states $|\mathbf{v}\rangle$ and $|\mathbf{v}'\rangle$ in a bright basis, separated by an energy ΔE and with a cumulative difference in node number for all modes equal to $n = |\mathbf{v}' - \mathbf{v}| = \Sigma|v_i' - v_i|$ (the '1-norm'). From a perturbation point of view, the mixing between them is given by

$$\mathscr{E} = V^{(n)}/\Delta E, \tag{3.1}$$

where the anharmonic coupling $V^{(n)}$ decreases exponentially with n (as discussed in detail in section 4). Both effects can be visualized simultaneously in quantum number space (figure 3.1). For a basis with $\mathcal{N}$ degrees of freedom, each state can be represented on a Cartesian lattice (QNS) as a point, the vibrational ground state being located at the origin. This picture is most applicable in anharmonic normal, local and normal mode bases; it requires modification for rotor modes (e.g. methyl groups) due to the different structure of rotor phase space (*vide infra*).

States near in energy lie close to a given energy shell (figure 3.1), while states near in nodal structure have a small value of n, equal to the 1-norm distance between the states. It is therefore immediately apparent which states are most strongly coupled: those whose connecting vector is short and has its largest components along QNS axes corresponding to small vibrational frequencies. Owing to the correspondence between quantum numbers and actions in units of $\hbar$, it also affords direct comparison with diffusion models of IVR (Schofield and Wolynes 1993, Wu 1996). Most detailed classical studies have been performed on small model systems, which show localized resonances (Fried and Ezra 1987, Kellman and Xiao 1990). Although overlapping resonances complicate the picture for large $\mathcal{N}$, or at high E, it will be seen that localized structure persists in IVR for several reasons.

One is the fact that IVR couplings are redundant. This is expressed in a 'vibrational

triangle rule' (Gruebele 1996c) discussed in more detail in section 4: among randomly chosen triplets of states, either all are strongly connected to one another or none. Different regions of QNS are thus exponentially separated from one another.

Another reason is illustrated by two extreme types of states found in QNS, closely related to the concept of 'extreme motion states' (Gambogi *et al.* 1993b). Edge states are located near the axes; their excitation is localized in one or a few modes and corresponds to (near) overtones. Interior states are located far from the axes, and correspond to high-order combination bands with somewhat more complicated nodal structure (Bigwood and Gruebele 1995b, 1997). There are generally fewer states with spectroscopic bright character (large transition moments with respect to $|0\rangle$) as one moves to the interior of QNS. In a typical experiment IVR therefore proceeds from the axes to the centre of the energy shell. When off-shell states participate extensively, IVR is termed off-resonant ('vibrational superexchange' (Stuchebrukhov *et al.* 1993)), otherwise it is resonant (Bigwood and Gruebele 1995b).

Edge states are less well connected to other states because they lack coupling opportunities, namely all the hypothetical states outside the first $2^{\mathcal{N}}$-tant (octant in figure 3.1) that would lie near them. Their average number of couplings is reduced by a factor of roughly $2^{\mathcal{N}}$ (Leitner and Wolynes 1996a, Pearman and Gruebele 1998a, see section 4).

Interior states are, in principle, better connected than edge states. However, there is a competing factor that can significantly reduce the IVR rate from interior states. In large low-symmetry molecules, the majority of modes become sufficiently localized such as to be effectively 'independent' from one another. This occurs most easily for hydrogenic stretching modes (Gambogi *et al.* 1993b, Pearman and Gruebele 1998a), but to a lesser extent even for backbone vibrations. This is illustrated schematically in figure 3.2 for two cases. For example, if energy E is deposited in an interior state $|n, n\rangle$ with two independent local modes populated, each will initially relax at a rate typical of an excitation energy $E/2$, which could be much slower than the rate of relaxation from $|2n, 0\rangle$ or $|0, 2n\rangle$. Similarly, if E is initially deposited in a specific mode, it may split into independent regions of the molecule governed by a rate $k(E') < k(E)$. 'Independence' specifically means that there are no anharmonic cross couplings in the potential between the modes in question. To what extent this condition is satisfied in smaller molecules requires more detailed considerations (Pearman and Gruebele 1998a) (see sections 4 and 6).

It is apparent from figure 3.1 that in a bright basis picture, the important density of states is not the total density of states ρ, but the local density of states $\rho_0^{(n)}$ of states on the energy shell a distance n away in QNS. The reason is that couplings scale according to equation (3.1): n, not just ΔE, enters as a parameter controlling coupling strength (sections 4 and 7). This is in keeping with chemical intuition that vibrational motions in well separated parts of a molecule (which are connected by chains of couplings) should not be strongly coupled.

3.3. *Prediagonalized bath*

The picture coupling a bright state to a prediagonalized bath was first used to point out the necessity of nonradiative transitions and IVR in polyatomic molecules (Bixon and Jortner 1968, Freed 1976a, b), and has been commonly used for about 30 years. As in section 3.2 (QNS), the bright state is chosen to carry all the oscillator strength. However, unlike in section 3.2, the bath is prediagonalized to an eigenbasis of H with one state projected out. Since the bath levels resemble the eigenstates of the full

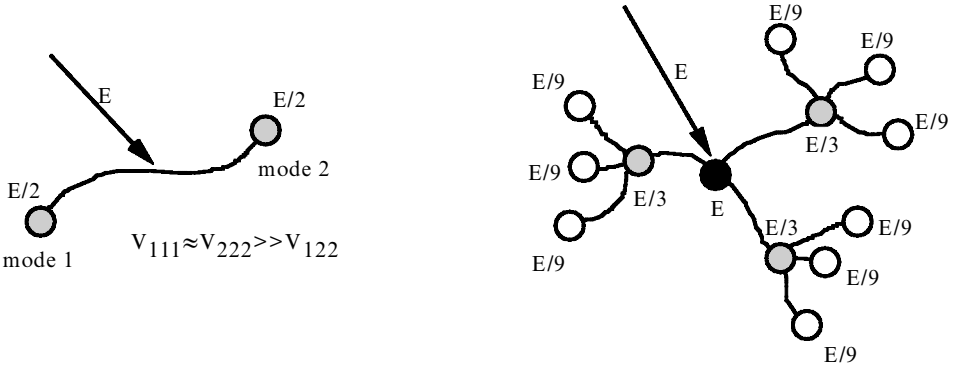

Figure 3.2. Two extreme cases of kinetic or distance localization. On the left, energy E is deposited into a combination band consisting of two localized excitations, which then undergo IVR at a rate corresponding to $E/2$ and a correspondingly lower density of states. In effect, the two halves of the molecule act independently starting at $t = 0$. On the right, the input energy excites a localized motion, which spreads into (partially) separated manifolds, each with a lower effective energy of excitation, increasing the timescale of IVR at each step. These effects can limit IVR in large molecules or intermediate-size chain molecules.

Hamiltonian H in their complexity, this representation effectively mixes the eigenstate and QNS (bright basis) pictures, picking a bright state representation for the initial state, and an eigenstate representation for the final states. Since the experimentally prepared feature looks like a bright basis state initially, then loses phase coherence to look like an eigenstate, the prediagonalized bath picture effectively switches pictures from 3.2 (QNS, early times) to 3.1 (eigenstates, long times). This is both its greatest strength and weakness.

The anharmonic coupling strength in this basis is distributed over a dense manifold of bath states, and is therefore small on average. In a matrix representation, k diagonal energies and $k-1$ off-diagonal matrix elements must be determined. This can be done directly from experiment using the LKL algorithm (Lawrance and Knight 1985, Lehmann 1991), since a high-resolution rotationless ($J = 0$) vibrational spectrum provides an equivalent representation with k transitions and $k-1$ relative intensities.

If the off-diagonal matrix elements V_α are small and uncorrelated (an often overlooked assumption), and if the density of prediagonalized states $\rho(E)$ is large and slowly varying across the transition width (Bixon and Jortner 1968), first-order perturbation theory (Golden Rule) may be applied to yield a rate and IVR survival probability

$$k_{\mathrm{GR}} = \frac{2\pi}{\hbar}\rho(E)V_{\mathrm{rms}}^2 \quad \text{and} \quad P(t) = P(0)\mathrm{e}^{-k_{\mathrm{GR}}t}. \tag{3.2}$$

In this formula ρ is the total density of vibrational states (in contrast to the local density of states $\rho^{(n)}$ to be introduced later), V_{rms} is the root-mean-squared coupling matrix element from the bright state to the prediagonalized bath, and k_{GR} is the well-defined Golden Rule rate for an exponential dephasing process. Such a formula cannot apply at very low energies where ρ is too small, as the couplings could be significantly smaller than the mean level spacing, and no meaningful rate can be defined.

It is not generally appreciated that equation (3.2) does not provide any mechanistic insight into molecular energy flow, but is simply a restatement of experimental

observation. The LKL algorithm provides a direct path from $k-1$ relative intensities and k spectral positions to the k diagonal elements and $k-1$ couplings V_α mentioned above. The rms average of the latter yields V_{rms}, while the mean spacing between the diagonal elements yield ρ. If the requirements of perturbation theory are met, then the rate (3.2) will of course match the experimentally observed linewidth from which it was derived. Furthermore, reducing the signal to noise ratio (SNR) will yield a smaller ρ, larger V_{rms}, and again the same rate. The only conserved dynamical variable is the rate k, while ρ and V_{rms} are measurement-dependent.

One could object that an experiment of high SNR can produce unbiased values of ρ and V_{rms}, and that is indeed true. However, our calculations in section 7 show that over a large fraction of the interesting energy range, polyatomic molecules do not explore all available phase space cells (i.e. Heller's $F < 1/3$) (Gruebele 1996c). This manifests itself in a significant fraction of IVR transitions of very low spectral intensity which could escape detection and artificially lower ρ. The problem is compounded by the fact that harmonic state counts also tend to yield low values, comparing favourably with experimental values, although both are lower bounds.

From a theoretical point of view, equation (3.2) poses similar problems. The prediagonalized manifold can presumably be computed from a known basis, in whose terms the Hamiltonian is well understood (e.g. a normal mode representation). Such calculations are nontrivial for large molecules, and if they have to be carried out, would obviate the need for a prediagonalized representation since it is no easier to diagonalize a $k-1$ dimensional manifold (bright state missing) than a k dimensional manifold. As seen in section 7, such explicit calculations generally verify that the assumptions of small V_α and large $\rho(E)$ are satisfied for larger molecules. However, the magnitudes of the V_α and their average V_{rms} are not related to anharmonic couplings in a known basis in a simple linear fashion. For example, it will be seen in section 7 that the assumption 'because the rate depends quadratically on V_{rms} it might depend quadratically on the average cubic anharmonicity $V^{(3)\prime}$ is entirely unfounded. Therefore the value of V_{rms} derived from an experiment provides no insight into well understood molecular parameters, but merely restates the observed properties of the spectrum.

There are also problems on the transitional timescale. The assumption of uncorrelated V_α is not generally satisfied (see section 7 and Bigwood and Gruebele (1995b, 1997)). If the V_α were uncorrelated, their fluctuations about the average V_{rms} could be modelled by drawing values at random from a distribution function, e.g. a normal distribution centred at $V_\alpha = 0$. The lineshape would then be a Lorentzian at high state densities. In reality, the local nature of anharmonic couplings (see sections 3.4, 3.5 and 4 and 7) leads to correlations in V_α which manifest themselves in terms of significant deviations of $P(t)$ from equation (3.2) at intermediate times. These deviations are not of the nature of quantum beats, which can occur at small ρ and short times in 'intermediate case' IVR spectra. They result in the fundamental inapplicability of exponential decay laws (figure 1.2) and the concept of a rate constant to the IVR process due to the nature of the Hamiltonian, which supports bright state features in addition to eigenstates. Due to these correlations, there is no simple theory for V_{rms} in terms of the spectroscopic cubic coupling constants $V^{(3)}$ (or higher than cubic couplings $V^{(n>3)}$).

In the limit where its perturbation assumptions are satisfied, the Golden Rule thus provides an accurate description of the dephasing rate of a feature. However, because it is still largely an eigenstate representation of the IVR problem (except for one single

state), it provides no computational help or mechanistic insight into IVR, other than that the lineshape should be Lorentzian *if* all couplings to the prediagonalized bath are uncorrelated and $\rho \to \infty$.

3.4. *Tier model*

Closely related to the previous two pictures is the tier model first proposed explicitly about 20 years ago (Freed 1976b, Muthukumar and Rice 1978, Quack 1983). It recognizes that even though $\rho(E)$ is large and V_{rms} is small in a prediagonalized basis, anharmonic or kinetic couplings in *most* bases are typically large (1–100 cm^{-1} for the lowest order terms) and the local density of directly coupled states is sparse. This results in a small number of couplings per state (section 4). Starting with a given bright state, a set of strongly connected states forms a first tier, another set of states connected to those a second tier, and so forth (figure 3.1).

The advantage of the tier model is that it can be applied to well characterized basis sets such as the normal mode representation. The couplings are thus well understood and can be directly estimated from spectroscopic anharmonicities or *ab initio* calculations (Friesner *et al.* 1993, Madsen *et al.* 1997). Classification of states can proceed either by the order of the coupling (Stuchebrukhov and Marcus 1993), or via a perturbation criterion (Bigwood and Gruebele 1995b). In effect, the tier model presents the QNS picture with energy as one axis, and similarity of nodal structure between basis states as the second axis. The only thing that must be kept in mind is that there can also be important couplings within tiers and across tiers, as is clear from the QNS picture. No simple tier model (i.e. a Cayley tree without loops) can fully describe the coupling structure of a bright basis.

Classification by order is similar in local, anharmonic normal, and normal mode bases. In the latter case, a suitable prescription would be 'tier $k+1$ consists of all states coupled to states in tier k by a term of order n or lower in the Hamiltonian', where n is usually 4. This type of scheme is ideal if IVR proceeds through chains of low-order couplings with off-resonant intermediate states, since such chains progress through the tier structure in a natural manner (figure 3.1). The order criterion simply recognizes that matrix elements tend to decrease exponentially with the quantum number difference (Parmenter 1983, Rashev 1990) of their constituent wavefunctions.

There are, however, cases when IVR becomes resonant, particularly when heavy-atom modes and low vibrational frequencies are involved (Bigwood and Gruebele 1995b, 1997, Pearman and Gruebele 1998a). As discussed in section 5, in such cases higher order direct couplings with $n > 4$ can dominate over low-order coupling chains after a critical time $\tau^{(n)}$. These couplings are therefore critical in establishing the dilution factor and F value for the IVR process.

Such cases are not well accounted for by order sorting, because high-order couplings are neglected. This can be remedied by using a perturbation criterion $\left|V_{ij}/\Delta E_{ij}\right|$, which selects states according to the mixing of wavefunctions in the two state approximation. Although this includes higher order couplings, it presents its own problem: pairs of states selected by such a scheme may be pushed apart by low-order interactions with distant states, while pairs missed by such a scheme may be pushed together (Pearman and Gruebele 1998a). The same phenomenon persists in the application of distorted wave operators (Iung *et al.* 1993, Maynard and Wyatt 1995). Section 5 discusses a sequential classification scheme which remedies this situation by coarse-graining the coupling structure: major low-order interactions among basis states are used to construct a new bright basis which has no IVR (fragmentation), but approximately correct line centre positions. The relationship between such coarse-

grained bright basis states and eigenstates is again the same as between a smoothed effective Hamiltonian and the full vibrational Hamiltonian with all 'unpredictable' resonances, as discussed in section 1.

The usefulness of classification schemes such as tier structures can be assessed by examining energy flow through the tiers. In many cases our calculations *without an imposed tier structure* show a clear temporal hierarchy, indicating the basic soundness of the idea (Bigwood and Gruebele 1995a, 1997). Whichever selection method is chosen, the main advantage of this model remains that it allows a direct connection of theories at a molecular level of detail with experiment.

3.5. *Bose-gas model*

A point of view which is particularly useful for merging molecular detail with a statistical treatment treats the vibrational quanta as a Bose gas, in analogy to black body radiation ((Gruebele 1996c), figure 3.1 and the Bose statistics triangle rule model in section 4). The cavity modes are replaced by $\mathcal{N}$ vibrational modes, and the photons by vibrational quanta. Vibrational quanta are allowed to fill the $\mathcal{N}$ modes with any occupation number, and can therefore be treated by Bose–Einstein statistics. This is appropriate for both thermal excitation and laser excitation, in which the temperature is replaced by a microcanonical β value.

This point of view is also helpful in the consideration of direct high-order couplings versus low-order coupling chains mentioned in the description of the tier model. It translates easily into symbolic manipulation of quanta for the calculation of the total and local densities of states necessary to examine the prevalence of different order couplings (section 4, low- versus high-order resonances).

3.6. *Rotor modes*

Internal rotor modes are not well treated by the QNS representation in 3.2. Classically, this results from a discontinuity in the phase space representation for pendular systems, which have a separatrix at the potential maxima. The best representation switches from vibrational operators a and $a\dagger$ to rotational operators j_i above the barrier. The zero-order energy level structure switches from vibrator tunnelling clusters to rotor levels with selection rules depending on the symmetry of the potential near equilibrium (e.g. threefold for methanol, onefold for H_2O_2) (Martens and Reinhardt 1990, Perry *et al.* 1995).

The zero-order structure can be reasonably well represented by connecting semiclassical formulae above (rotor modes) and below (vibrator modes) the barrier height H. This mapping is illustrated in figure 3.3 for the onefold case with the result that (Pearman and Gruebele 1998b)

$$\begin{aligned} E_n^{(0)} &\approx \left(\frac{E_v^2 + R^2 E_r^2}{1+R^2}\right)^{1/2} \\ E_v &= 4\omega\left\{j - \left[1 - \frac{1}{4}\left(\frac{B}{H}\right)^{1/2}\right] + \frac{1}{4}\right\}^2 \\ E_r &= \{Bj^2 + H/2\}^2 \\ R &= \exp[2Bj^2/H] - 1. \end{aligned} \tag{3.3}$$

Couplings between pairs of states either both below or both above the barrier follow the same rules (derived in section 4) for vibrator modes, except that rotor mode couplings scale with a Born–Oppenheimer parameter a^2 instead of a if expressed in

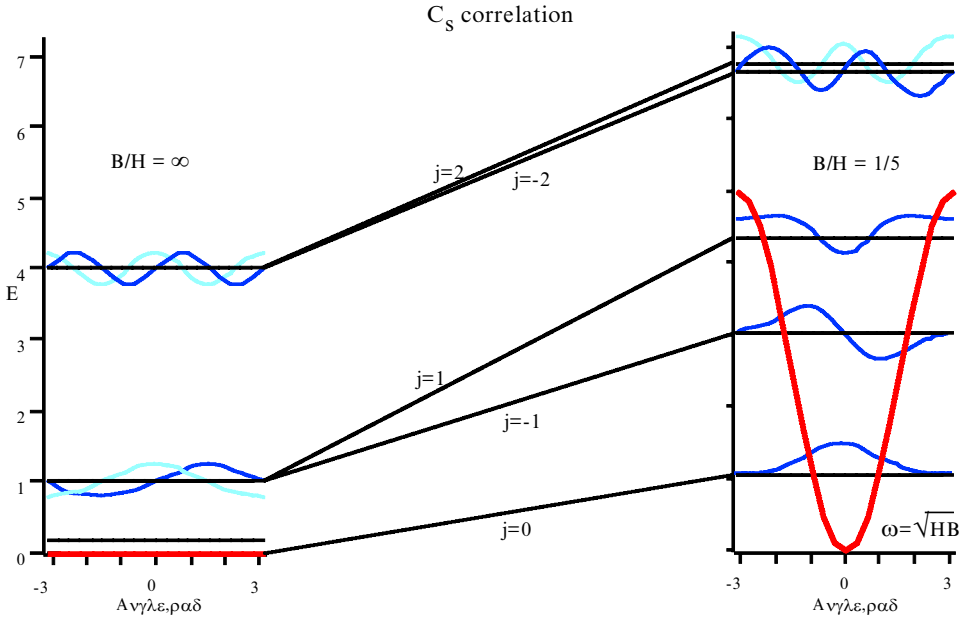

Figure 3.3. Rotor correlation diagram for the C_s case for $B/H = \infty$ to $B/H = 1/5$. B is the rotor rotational constant, and H is the barrier height.

terms of Δj (the one-dimensional (1D) rotor quantum number difference) instead of Δn (the 1D vibrator quantum number difference) (Oka 1967).

The situation is more complex for couplings connecting states near the barrier or across the barrier. In that case, the vibrator basis must be expanded in terms of the rotor basis, yielding a distribution of m states contributing each n state. These distributions can be parameterized in terms of the mode energy E_{torsion} and the quantity B/H, where B is the rotational constant of the internal rotor. The important fact is that in the near-barrier case, internal rotation can induce multiple quantum transitions with large jumps in quantum number in either the vibrator or rotor representation: it becomes 'intrinsically' off-diagonal in any bright state picture.

The result (section 7) is that couplings between states near the barrier are enhanced, while couplings high above the barrier decrease rapidly, leading to an isolation of the rotor mode (Pearman and Gruebele 1998a).

4. State couplings

Two ingredients are required for detailed calculations of IVR : an efficient way of generating the molecular Hamiltonian, and an efficient way for computing the dynamics of this Hamiltonian in the energy or time representations. In this section we consider the first of these.

Ab initio calculations and fits to experimental data are the most accurate ways of treating the molecular Hamiltonian. The main drawback of these approaches is their computational expense when applied to systems with many degrees of freedom. *Ab initio* surfaces for tetra- or pentatomic systems and six-dimensional (6D) dynamics are currently the state of the art in scattering calculations (Munn and Clary 1996). Full 6D fits to experimental data are currently the state of the art for adaptation of potential surfaces to experimental data (Burleigh *et al.* 1996, Qiu and Bacic 1997, Bigwood *et al.* 1998). We will discuss an application of these approaches in section 8 in conjunction

with experimental measurements on $SCCl_2$. Here we turn to methods which are more easily extensible to large systems with more than nine degrees of freedom.

In IVR dynamics, the detailed fragmentation pattern of a spectrum or the exact nature of small quantum beats, are often not of interest. Instead, one wishes to calculate averaged quantities such as the IVR rate at early times, the dilution factor, the functional form of $P(t)$ at transitional times, the spectral intensity fluctuations, or the level spacings. This does not necessarily imply that the molecule is completely in some statistical limit such as the GOE (Brody *et al.* 1981), but statistical simplifications can nonetheless be applied.

We consider a systematic way in which such simplifications of the Hamiltonian can be derived in the energy representation for use in dynamical calculations (section 5). The method will be illustrated mainly for the normal mode basis, with a brief discussion of other basis sets (local, diagonal anharmonic) which show similar behaviour when treated statistically. The models illustrated here cover a range of detail, allowing one to 'tune' how much molecular specificity is to be retained. The most complete models can provide excellent agreement with experiment, as discussed in examples in section 6.

4.1. *Scaling of the Hamiltonian*

It has long been recognized that matrix elements of vibrational operators in the normal mode representation decrease exponentially with the quantum number difference between the wavefunctions (Oka 1967, Parmenter 1983, Bullock *et al.* 1990). This arises naturally if the terms in the Hamiltonian are separated into potential constants in *energy units* and unitless position operators written in terms of ladder operators, $q = (a^\dagger + a)$. A matrix element can then be written as

$$\langle \mathbf{v}' | V(\mathbf{q}) | \mathbf{v} \rangle \approx V^{(n)}_{\mathbf{v}',\mathbf{v}} = \langle v_1, v_2 \cdots | V^{(n)}_{\mathbf{n}} \prod_{i=1}^{\mathcal{N}} q_i^{n_i} | v_1, v_2 \cdots \rangle = V^{(n)}_{\mathbf{n}} \prod_{i=1}^{\mathcal{N}} \langle v_i | q_i^{n_i} | v_i \rangle, \qquad (4.1)$$

where the potential constant $V^{(n)}_{\mathbf{n}}$ decreases exponentially with $n = \Sigma n_i = \Sigma |v_i' - v_1|$. The approximation after the first term arises because nth order matrix elements also have contributions of order $n + m$ where $m = 2, 4, 6 \cdots$. These generally amount to less than 10% of the total value of matrix elements except in the cases $n = 1$ or $n = 2$ (Madsen *et al.* 1997).

Scaling is a direct consequence of the Born–Oppenheimer approximation and the resulting definition of the ladder operators; in fact, the magnitude of the couplings $V^{(n)}_{\mathbf{v}',\mathbf{v}}$ depends on n as

$$V^{(n)}_{\mathbf{v}',\mathbf{v}} \approx V^{(3)} a^{n-3} \bar{v}^{n/2}_{\mathbf{v}',\mathbf{v}} \qquad (4.2)$$

where a is typically about 0.1, and $\bar{v}_{\mathbf{v}',\mathbf{v}}$ is a geometrically weighted distance in QNS between states $|\mathbf{v}\rangle$ and $|\mathbf{v}'\rangle$ (Bigwood and Gruebele 1995b, Madsen *et al.* 1997). This scaling behaviour is universal in the sense that the same scaling with slightly different values of a is retained as long as a bright basis is used.

The invariance of the scaling in different simple coordinate representations is due to the virial theorem: kinetic and potential terms of a weakly anharmonic potential ($a < 0.2$) are always weighted about equally in the total energy. Unitless momentum operators $i(a^\dagger - a)$ lead to the same scaling as equation (4.2) for coordinates. Whether mode couplings are kinetic, potential, or any combination thereof, a power series expansion always leads to a power law ordering of the couplings with n. Although the details of the coupling structure must of course differ, the overall appearance of the

Hamiltonian matrix in all of these representations is governed by exponentially scaled matrix elements of magnitude given by (4.2).

As a result of the coupling structure, high-energy eigenstates of large low-symmetry molecules appear to be random admixtures of basis states due to multiple resonances, while features obtained by summing eigenstates under a spectral envelope have a simpler structure well represented by a few bright basis states. The fact that such features exist at all is due to the small ratio a^{n-2} of nth order anharmonic constants to the quadratic term in the potential energy surface (PES), i.e. the fact that the Born–Oppenheimer approximation for covalent bonds leads to well-defined potential minima and a dissociation limit much larger than typical vibrational frequencies. As stated in section 1, 'unrelaxed' features are remnants of the $a \to 0$ limit of the vibrational Hamiltonian.

Since IVR is simply the evolution of bright states into a phase-decorrelated sum of eigenstates, at long times all 'bright state bases' must show qualitatively similar behaviour. In that sense, conclusions from the couplings represented in such a basis are also universal at long times or for averaged quantities. At short times, IVR is more sensitive to the details of the anharmonic coupling structure, and one or another 'bright state basis' may be the best zeroth-order approximation, but any of them provides a compact description of the initially excited feature state.

4.2. *Factorization of the Hamiltonian*

In addition to the trivial factorization of the coordinate part of the matrix element in equation (4.1), it is less obvious that the potential constants $V_{\mathbf{n}}^{(n)}$ themselves can be logarithmically (product) expanded as

$$\left|V_{\mathbf{n}}^{(n)}\right| = \prod_{i=1}^{N}\left[\left(\frac{V_i^{(3)}}{a_i^3}\right)^{n_i/n} a_i^{n_i}\left[\prod_{j>i}^{N} c_{ij}^{(2)n_i n_j}\left[\prod \cdots\right]\cdots\right]\right]. \tag{4.3}$$

Under certain assumptions, it can be shown that the first product completely describes potential constants as the number of vibrational nodes $\mathcal{N} \to \infty$ (Madsen *et al.* 1997). The first term in equation (4.3) can therefore be viewed as an asymptotic description of the PES which reduces all potential constants, whose number grows exponentially with order n, to $2\mathcal{N}$ parameters $V_i^{(3)}$ (diagonal cubic potential constants) and a_i (Born–Oppenheimer parameters for each vibrational mode).

This description can be quite accurate for highly connected molecules even when $\mathcal{N}$ is small, as seen in a comparison of factorized potential constants and a four correlated pair generalized valence bond (GVB) calculation for $SCCl_2$ in figure 4.1. Furthermore, it is quite sufficient for the purpose of calculating initial IVR decay rates and dilution factors and following trends as a function of molecular size, mode frequencies, etc. It is also competitive with *ab initio* calculations for high-order ($n > 4$) constants, where even good surfaces are not likely to predict individual potential constants to better than a factor of two (Madsen *et al.* 1997). The main drawback of equation (4.3) is that it fails to predict the signs of potential constants. It has been shown that for the purposes of IVR, these can be assigned randomly with good results, based on comparison with the statistical distribution of signs derived from coordinate potential surfaces (Gruebele 1996c, Pearman and Gruebele 1998a).

For molecules of lower connectivity (e.g. chain molecules) or with large atomic mass disparities, the higher terms in equation (4.3) also become important (Pearman and Gruebele 1998a). The coefficients $c_{ij}^{(2)}$ decorrelate pairs of modes from one

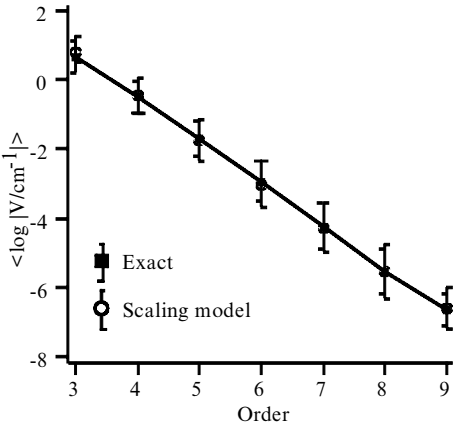

Figure 4.1. Comparison of *ab initio* ('Exact') and factorization/scaling predictions for $SCCl_2$. Shown are average potential constant magnitudes and second moments of their distribution (left-hand and right-hand bars) as a function of order n.

another, and can be evaluated approximately from a bond distance matrix and a normal coordinate analysis of a specific molecule. The latter takes into account mass effects (e.g. the idea that a very heavy atom will partition the molecular phase space into quasi-independent parts), while the former takes into account the localization of electron-pair bonds between atoms (e.g. the idea that local structural changes in non-aromatic molecules lead to additive changes in the total energy). Figure 4.2 shows the distribution of $c_{ij}^{(2)}$ averaged over many organic molecules. While much of the distribution corresponds to values < 1 (decreasing the potential constants in equation (4.3)), some $c_{ij}^{(2)}$ also exceed 1, although they never exceed $1/(a_i a_j)$, which would lead to divergence of equation (4.3).

In sections 6, 7 and 9 we will predominantly use the simple PES model discussed here. For transition-by-transition comparisons with small molecule experiments (section 8), *ab initio* approaches will also be considered. The advantage of the factorization method is that high-order couplings can be treated economically in large molecules; its disadvantage compared to *ab initio* methods is that individual low-order couplings are not represented with enough ($\ll 50\%$) accuracy to quantitatively predict spectral features of small high-symmetry molecules such as acetylene.

4.3. *Low-order versus high-order resonances*

An important question which has not been systematically discussed in the past is the relative contribution to IVR of low- and high-order resonances, and of direct (resonant) and indirect (off-resonant) coupling paths in a well-defined basis representation. (Indirect coupling paths are 'chains' connecting two states via a third or more intermediate states, as in Stuchebrukhov *et al.* (1993).) These are critical factors in localization as they define what types of 'jumps' are required in QNS to yield energy redistribution.

Direct low-order couplings must clearly dominate at low energies over direct high-order couplings, but at high energies and density of states this role is reversed. High-order couplings become important for several reasons: the higher local density of states offsets their smaller magnitude at high energies or in larger molecules; they grow faster in number with increasing energy and $\mathcal{N}$; they are weighted more due to the

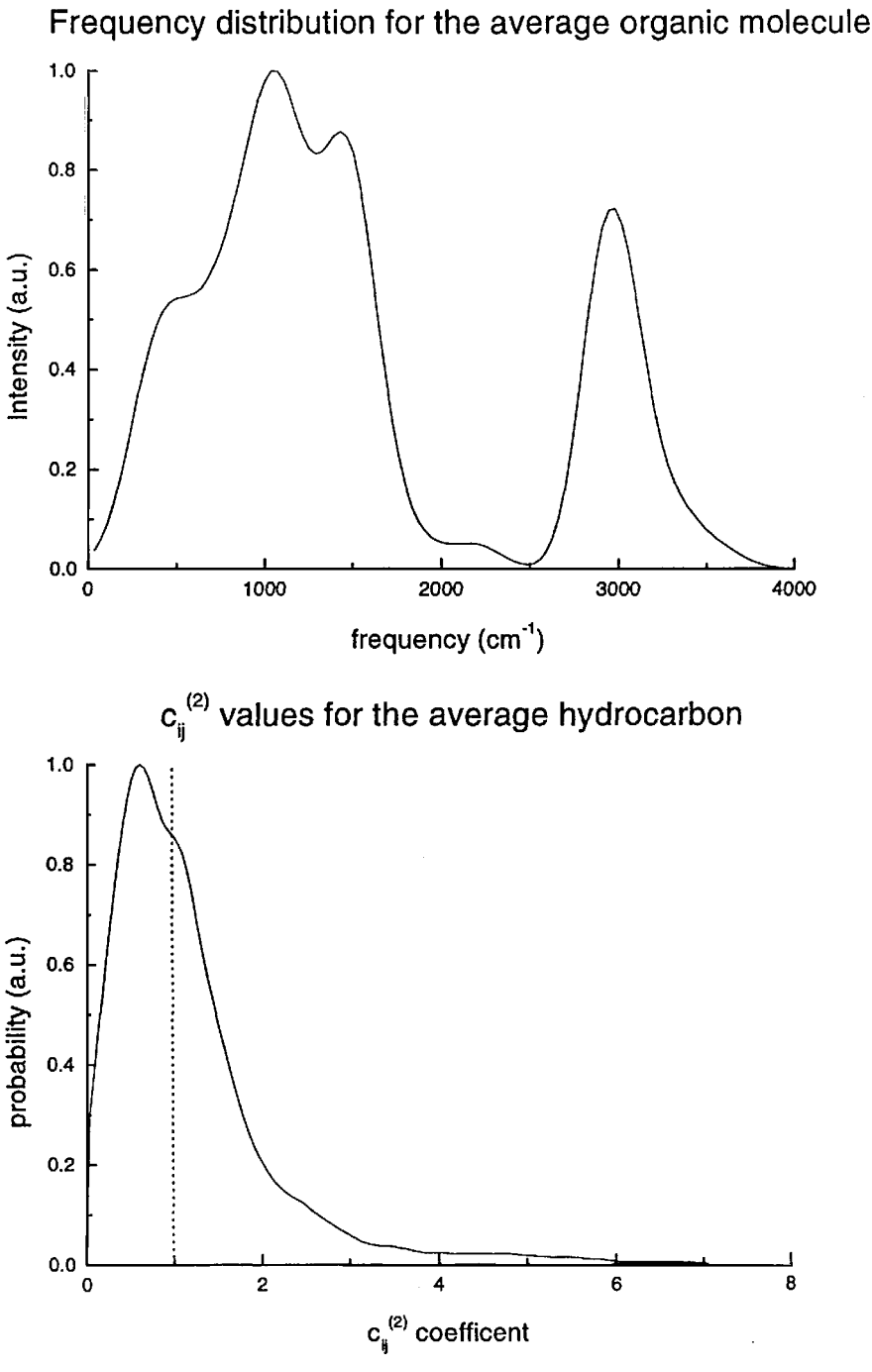

Figure 4.2. Frequency power spectrum and distribution function of $c_{ij}^{(2)}$ coefficients for an average of many organic molecules. The $c_{ij}^{(2)}$ values include effects of kinetic/distance localization, which are more subtle in most molecules than implied by the diagrams in figure 3.2.

larger $\bar{v}^{n/2}$ factor in equation (4.2) (Bigwood and Gruebele 1995b, Madsen *et al.* 1997, Pearman and Gruebele 1998a).

Semiclassically, a model for IVR via high-order resonances has been described by Heller (Heller 1995). Here, we focus on an analysis of such couplings using the QNS picture (figure 3.1) and quantum mechanical matrix elements in equations (4.1)–(4.3). Both numerical simulations and analytical models show that direct high-order resonances exceed direct low-order resonances as the vibrational energy and $\mathcal{N}$ are increased, due to the faster growth in their numbers. The number of states directly coupled to order n scales as $E^{n/2}$ at sufficiently high energies (Madsen *et al.* 1997, Pearman and Gruebele 1998a). There is a value $n_{\max}$ of the order of couplings which need to be included, which is ≈ 4 at low energies, but can exceed 6 at high energies. For example, $n_{\max}$ is 4 for $SCCl_2$ up to 6000 cm^{-1}, and $n_{\max}$ is 5 between 6000–9000 cm^{-1}.

It is far less obvious that matrix elements of order $n > 4$ (e.g. quintic) also dominate over coupling chains of order $n+2 = n_1 + n_2$ (e.g. cubic plus quartic). On the one hand, the coupling chains grow faster in number than direct couplings by a factor of $\mathcal{N}$. On the other hand, anharmonic potential constants multiplying these chains have quasi-random signs (Pearman and Gruebele 1998a). The quasi-random signs therefore associated with the coupling chains lead to phase cancellation. For coupling chains involving p steps, the effective coupling increases nearer to $p^{1/2}Va^{n_1+n_2}$ (random walk result for identical couplings) than to $pVa^{n_1+n_2}$ (all signs the same) (Pearman and Gruebele 1998a). Extensive numerical simulations treating the coupling chains as random walks in QNS show that the importance of higher order couplings is sensitive to the energy gap ΔE_{ij} between two states being coupled, and to the parameters V_i and a_i. Due to an exquisite cancellation of number growth and phase cancellation effects, their importance depends much more weakly on the vibrational energy and size of the molecule, except in the trivial sense that a higher density of states favours the small direct couplings at small energy gaps (Pearman and Gruebele 1998a).

The average energy gap $\Delta\bar{E}$ in which higher order couplings (fifth and sixth) dominate over low-order chains is generally of the order of a few wavenumbers, corresponding to timescales of a few picoseconds or longer. Indeed, numerical simulations show that while neglect of higher order couplings does not affect the very short time IVR, their neglect affects IVR in the 'transition regime' and leads to drastic (greater than a factor of two) underestimates of dilution factors which characterize IVR in the long time limit (Madsen *et al.* 1997); see section 6.3. The number of states coupled to a given state by direct nth order couplings can be estimated using

$$N_1^{(n)} \approx \rho_0^{(n)} \Delta\bar{E}, \tag{4.4}$$

where $\rho_0^{(n)}$ is the local density of states separated by n quanta from the state in question (Pearman and Gruebele 1998a). Similarly, the contributions of coupling chains of length m and overall order n can be represented by a unitless effective number of coupled states $N_m^{(n)}$ (Pearman and Gruebele 1998a). The total effective number of coupled states is then given by

$$N_{\text{coupled}} = \sum_{n,m} N_m^{(n)}. \tag{4.5}$$

These quantities take into account both the local density of states and the coupling strengths $V_{v',v}^{(n)}$, and should be used as the parameter against which IVR dilution factors are plotted, rather than the total density of states.

4.4 *The Bose statistics triangle rule (BSTR) model*

We conclude our discussion of models with a statistically based simplification of the Hamiltonian matrix. Equation (4.1) is a simplification of the molecular PES, but still requires knowledge of all basis state quantum numbers $\mathbf{v}$ and $\mathbf{v}'$. The resulting IVR matrices or propagators are entirely non-statistical, although the matrix elements are only approximate.

At high energies, many of the features of IVR can be captured if the basis state manifold itself is treated statistically. An extreme form would be to apply the GOE (Brody *et al.* 1981). Even for an exponential distribution of off-diagonal elements, terms farther from the diagonal eventually can be mimicked by such an ensemble. However, except for the very highest energies, molecular IVR does retain some memory of the coupling structure, and cannot be described by the GOE ensemble (see section 6.2) (Gruebele 1996c).

The BSTR model (Gruebele 1996c) makes somewhat milder assumptions, and appears similar to GOE only in the limit as $a \to 1$. It has two main ingredients as follows.

(1) Off-diagonal matrix elements are given by equation (4.2), the values of n being normal-distributed with

$$\bar{n} \cong \frac{\underline{E}_{\text{eff}}}{\overline{\omega}} \tag{4.6}$$

$$\sigma_n^2 \cong \frac{2}{\mathcal{N}} \frac{\underline{E}_{\text{eff}}^2}{\overline{\omega^2}}. \tag{4.7}$$

Here $\underline{E}_{\text{eff}}$ is the available vibrational energy with a zero-point correction and $\overline{\omega}$ and $\overline{\omega^2}$ are harmonically averaged molecular frequencies and square frequencies (Gruebele 1996c).

(2) The coupling structure obeys a triangle inequality

$$|n_{12} - n_{23}| \leqslant n_{13} \leqslant |n_{12} + n_{23}|, \tag{4.8}$$

where n_{ij} is the quantum number difference between states i and j.

This vibrational triangle rule (VTR) leads to a more subtle localization of energy flow than simple kinetic isolation or spatial isolation possible in larger molecules (figure 3.2). In effect QNS regions are either coupled by several strong couplings or not at all, reinforcing the strong couplings (Gruebele 1996c). In reality, this triangle inequality is only a propensity rule: higher order contributions to matrix elements are sometimes significant (particularly for $n = 1$ or 2, which correspond to cubic or quartic terms in a normal mode representation); furthermore, not all the potential constants of a given order are even approximately equal in magnitude (figure 4.1). However, numerical simulations using an *ab initio* PES for $SCCl_2$ have shown that (4.8) still holds for greater than 90% of state triplets when accurate potential constants are used (Gruebele 1996c).

We will use this model on several occasions where only averaged results are of interest. Even in this simple form however, the model retains information about molecular size and frequency distribution via parameters such as $\mathcal{N}$, $\overline{\omega}$ and $\overline{\omega^2}$ in equations (4.6) and (4.7).

5. Computational methods

5.1. *Level selection*

Bright state representations of H are not necessarily efficient, even with the exponential scaling of matrix elements. As discussed above, the smaller couplings cannot be neglected if long time information is desired. Furthermore, the exponential growth in the density of vibrational states as energy increases is unavoidable. Since quantum dynamics is an NP class problem, the number of vibrational levels within a reasonable energy window quickly becomes intractable even on fast large-memory computers as one approaches energies where interesting dynamics can occur.

Fortunately, only a fraction of the total vibrational ensemble need be included in any numerical simulation to obtain converged results at short to transitional times, and in some cases at long times. The key is to identify these states *before* the memory critical step of assembling the Hamiltonian matrix or propagator. In the following paragraphs we discuss two closely related level selection algorithms we have developed to address this problem (Bigwood and Gruebele 1995b, Bigwood *et al.* 1998).

The first is based on a simple two-level perturbation criterion that is applied in a tier-like fashion beginning from the spectroscopic bright state. In the first tier, all states within a specific bandwidth are compared to the bright level and given a mixing weight,

$$\mathscr{L}_{v',v} = \frac{1}{[1+(E_{v'}-E_v)^2/V_{v',v}^2]^{1/2}}, \tag{5.1}$$

where the E_v are the energies of the states being examined and $V_{v',v}$ is the matrix element that couples them. The Lorentzian weight does an excellent job of describing the roll-off of mixing between states and can be sequentially multiplied through the chain of tiers to give an upper limit of the spectral bandwidth (figure 5.1), (Bigwood and Gruebele 1995b, Pearman and Gruebele 1998a). All levels with weights greater than some threshold value (typically .001 to .01) are selected as first-tier states. This process continues for subsequent tiers with previously unselected levels being compared to levels in the most recent tier, until some maximum number of tiers is reached (typically between five and ten).

While this method and similar ones (Wyatt *et al.* 1992, Zhang and Marcus 1992, Stuchebrukhov *et al.* 1993) have proven efficient enough to be used for many calculations, such as the low-lying overtones of propyne (Bigwood and Gruebele 1997) and several overtones and combination bands of $SCCl_2$, there are a few critical multi-level interactions that are not well addressed by a simple two-level picture. This is illustrated in figure 5.2.

Using the two-level scheme above with a cut-off greater than 0.1 and one tier, the algorithm would select only the lower two levels, and result in a spectrum with two strong transitions. Diagonalization of the full matrix would have yielded only a single transition because the middle level would have been pushed out of range by its own first tier state. The Distorted Wave Operator method (Iung *et al.* 1993, Maynard and Wyatt 1995) has a similar problem due to perturbation nonconvergence. Although the above example is extreme, less severe but similar situations occur frequently in real molecules. Equation (5.1) either misses important couplings or adds in unnecessary couplings if the cut-off is set too small.

The problem is exacerbated in bright state bases, where the couplings reflect the full anharmonicity of the potential surface. At higher energies, such as those in the thiophosgene molecule discussion in section 6, spectral features can be shifted by a few

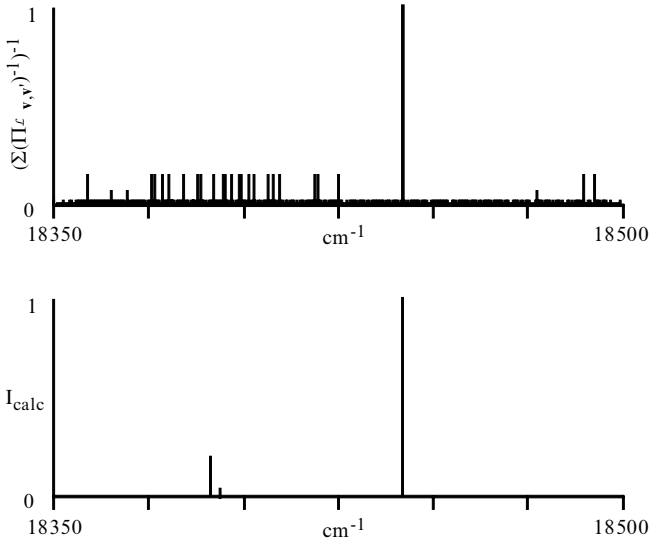

Figure 5.1. Comparison of the actual spectrum (lower diagram) with the perturbation selection criterion (upper diagram, sum over all paths of all the products along coupling chains weighted by the mixing criterion in equation (5.1)). The selection criterion is a conservative spectral predictor which includes all states that make a significant contribution to the final spectrum.

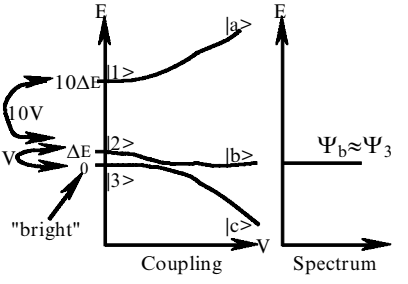

Figure 5.2. A bright state $|3\rangle$ predicted to mix with $|2\rangle$ by a perturbation criterion in fact produces only a single line in the spectrum, due to the fact that $|1\rangle$ pushes $|2\rangle$ out of resonance.

hundred wavenumbers from the structurally closest basis state. Although a diagonal anharmonic basis helps with overtones, it still results in many 'accidental' resonances. Experimental features (Nesbitt and Field 1996) are more directly related to such basis functions, but they do not greatly simplify IVR calculations, where the progression to dephased eigenstates is of interest.

To address this type of problem, we use the following variational enhancement of equation (5.1). (Bigwood *et al.* 1998). At each tier level, the mixing factor is applied to all levels within a large energy window (at least several times the highest vibrational frequency of the problem), using a very conservative cut-off value. One is left with a subset of 'candidate' levels that *may* participate in the dynamics.

In the next step, a correction to the zeroth order energy of each of the candidate levels is calculated by selecting the most strongly coupled 'pusher' states (typically about 20–200). For example, for a harmonic overtone $v = 8$ basis function, these include the $v = 6$, 7, 9, 10 overtone functions and a few other strongly coupled basis

states. Since we are interested only in approximate energy shifts, only one or two tiers of pusher states are used with a high cut-off criterion ($\approx .1$). The resulting matrix containing the candidate and its pusher states is diagonalized to give an improved estimate of the candidate's final energy.

Finally, the perturbation criterion is once again applied to the candidates, but now using their adjusted energies, which allows the use of a less conservative ($\approx .01$ to $.03$) cut-off value. If a candidate passes this final test, it and all of its pusher states are included in the final matrix. This results in a 2–4-fold reduction of final matrix size, or an 8–64-fold improvement in speed for the same accuracy.

This scheme effectively applies criterion (5.1) to a new set of $\Delta E_{v',v}$ values which have been shifted such that the important higher order interactions are readily apparent. Another way of looking at it is that a normal mode basis is transformed into an alternative bright basis corresponding to a better smoothed effective Hamiltonian (equation (1.5)), but whose states do not yet show fragmentation of features into eigenstates that would result from application of the full Hamiltonian.

Once the appropriate levels are selected, the sparse Hamiltonian matrix is assembled using the same perturbation criterion to determine which matrix elements should be included. It is important to note that in the end, there is no tier structure imposed on the matrix. Each level has the potential to be coupled with every other level, if the matrix element passes the cut-off test (5.1). The resulting matrix has a cluster-like topology due to the triangle propensity rule (Gruebele 1996c).

Pure dephasing spectral linewidths and survival probabilities are related by the Fourier transform relationship. They are, in principle, determined equally well from either time or frequency domain computations. In practice, time domain computations can be considerably faster at the expense of uncertainties in the eigenstate energies and intensities. There is, however, a rich pallet of more subtle phenomena that reveal much more detailed information about the IVR mechanism, and can be most easily extracted from one or the other computational method. For example, information about the state space localization of individual molecular eigenstates is best obtained by performing full frequency domain diagonalizations. Direct calculation of the temporal flow of amplitude through the basis states, or inclusion of short laser pulses in IVR simulations is most easily addressed with time domain computations. We have developed new numerical methods for both approaches.

5.2. *Frequency domain: Lanczos*

The Lanczos matrix diagonalization algorithm lends itself exceptionally well to the problem of large sparse matrices characteristic of molecules undergoing IVR (Nauts and Wyatt 1984). The algorithm itself is based on a simple recursion, that, in infinite precision, generates a set of orthogonal Ritz vectors and coefficients that tridiagonalize the Hamiltonian matrix (Cullum and Willoughby 1985).

Due to the finite precision of computations, there is a loss of orthogonality as the algorithm proceeds. If all eigenvalues are to be extracted, the tridiagonal Lanczos matrix must be larger than the Hamiltonian matrix by some multiplicative factor that grows with the system size. The eigenvalues generally appear as a function of Lanczos matrix size with a rate roughly governed by the overlap of their eigenvectors with the Lanczos starting vector, and their position in the matrix: eigenvalues in the wings tend to appear more quickly than those in the centre. This can be circumvented by remapping the Hamiltonian (Wyatt 1995). Eigenvectors of the Lanczos matrix can be obtained by inverse iteration, which is particularly fast for a tridiagonal matrix with

well converged eigenvalues. Eigenvectors of the Hamiltonian matrix require back transformation, i.e. multiplication of the Lanczos eigenvector by the entire set of Ritz vectors. With computer memory already strained by the size of the molecular Hamiltonian matrix, it is impractical to store these vectors, and they must be regenerated at a great penalty in speed.

We have implemented three major enhancements to the basic algorithm to improve its efficiency (Bigwood and Gruebele 1995b). The first is an adaptive Lanczos matrix size. Since, in practice, extracting the last ten per cent of the eigenvalues frequently requires a Lanczos matrix more than twice as large as that required for the first ninety per cent, it is efficient to gradually ramp up the matrix size. This way, the back transformation of the bulk of the eigenvectors requires only a minimal number of Ritz vectors.

Yet more speed can be gained by batch processing of the eigenvectors. In our implementation, any memory remaining after storage for the Hamiltonian matrix is used to store Lanczos matrix eigenvectors. The Ritz vectors need only be regenerated once for each batch of eigenvectors, yielding an improvement in overall speed by a factor of three to four if 25 vectors can be stored.

The third and final enhancement is the use of fully filled or multiple orthogonal random starting vectors for the Lanczos recursion. In light of the fact that the appearance of eigenvalues depends on their overlaps with the starting vector, improvements can be gained by restarting the algorithm with a new random vector rather than increasing the size of the Lanczos matrices to extract the last few eigenvectors. This is particularly true for weakly coupled systems.

5.3. *Frequency domain: matrix fluctuation–dissipation (MFD)*

If only a spectrum with m intensities is required, it should not be necessary to have the full m^2 eigenvector components of the diagonalized Hamiltonian. Rather, a 'sideways' diagonalization algorithm that picks out only one component of each eigenvector is sufficient. This is precisely the purpose of the matrix fluctuation–dissipation (MFD) algorithm (Gruebele 1996a), which can be thought of as a nonrecursive formula for the spectral residues (Gruebele 1996b).

The MFD theorem relates the spectral intensities to the susceptibility of energy eigenvalues to changes in the bright state coupling matrix elements:

$$|\langle n|0\rangle|^2 = \frac{1}{2}\frac{1}{E_n - E_0^{(0)}}\frac{\partial E_n(\lambda)}{\partial \lambda}\bigg|_{\lambda=1}, \tag{5.2}$$

where $|n\rangle$ is the eigenstate with energy E_n, $|0\rangle$ is the spectroscopic bright state with energy $E_0^{(0)}$, and λ is a scaling parameter that is applied to the direct couplings between the bright and bath states. As this method can be recast in the form of Green functions, it is in the same family as the RRGM method (Wyatt 1989). It should be noted that phase information (the signs of the eigenvector coefficients) is not provided. This presents no problem for the calculation of survival probabilities, due to the symmetry of the propagator.

Numerically, all that is required are two eigenvalue computations, which can be performed using Lanczos or any other large eigenvalue method such as Sturmian sequencing, with far less cost than a full eigenvector calculation. In the case of the Lanczos method, since only eigenvalues are required, the two back transformation related enhancements are of no use, but the use of multiple Lanczos starting vectors offers an increase in efficiency for some systems.

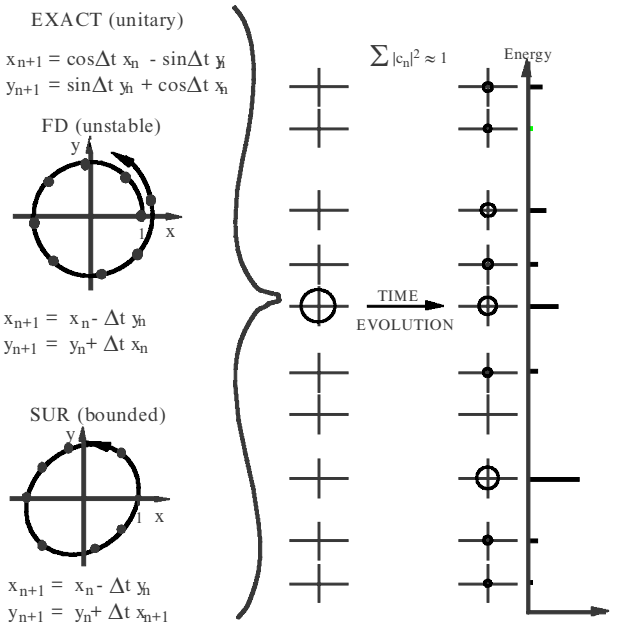

Figure 5.3. SUR propagator. Top left: exact unitary propagation for a single level; middle left: unstable forward differencing; bottom left: SUR immediately updates x_n before calculation of the imaginary part y_{n+1}. Geometrically, this algorithm can be thought of as distorting the correct circular phase rotation into an ellipse, without secular magnitude errors. Right: evolution of the phase circles with time produces the bright state spectrum upon Fourier transform.

5.4. *Time domain: shifted update rotation (SUR) and symplectic propagators*

Time domain IVR calculations demand a propagator for the Schrödinger equation that is stable, accurate over many characteristic system periods $\tau(P(\tau) = 1/e)$ and also memory efficient. Shifted update rotation (SUR) (Bigwood and Gruebele 1995a) is a member of the class of symplectic propagators which can be adapted for quantum mechanical propagation (Gray and Verosky 1994). The basic algorithm is a small but effective modification to the forward differencing method which, for a many-level coupled Hamiltonian system, can be represented as

$$c_j^{(r)}(t+\Delta t) = c_j^{(r)}(t) + \Delta t \sum_i H_{ij}^{(r)}\, c_i^{(i)}(t) \qquad (5.3a)$$

$$c_j^{(i)}(t+\Delta t) = c_j^{(i)}(t) - \Delta t \sum_i H_{ij}^{(r)}\, c_i^{(r)}(t+\Delta t), \qquad (5.3b)$$

where the c's are the real and imaginary parts of the system state vector, and the H_{ij}'s are the real matrix elements of the Hamiltonian. Unlike forward differencing, which uses $c^{(r)}(t)$ in equation (5.3b), SUR is area conserving, although not unitary (figure 5.3). SUR does not require any temporary storage vectors. Its phase error increases quadratically in time, making it very competitive with standard algorithms at short to intermediate times (Feit *et al.* 1982, Kosloff and Kosloff 1983, Tal-Ezer and Kosloff 1984) when a sparse energy representation can be applied. This is very important in IVR calculations out to a few 100 ps, since methods such as the BSTR require many shorter calculations to allow for statistical averaging.

While SUR is slower than some of the other symplectic integrators (Gray and Verosky 1994), it is distinguished by the fact that it maintains its stability even in the presence of complex valued, time-dependent matrix elements κ_{ij}, for which the algorithm becomes

$$c_i^{(\mathrm{r})}(t+\Delta t) = c_i^{(\mathrm{r})}(t) + \Delta t \sum_j \{H_{ij}^{(\mathrm{r})} + \kappa_{ij}^{(r)}(t)\} c_j^{(\mathrm{i})}(t) + \Delta t \sum_j \{H_{ij}^{(\mathrm{i})} + \kappa_{ij}^{(\mathrm{i})}(t)\} c_j^{(\mathrm{r})}(t) \tag{5.4a}$$

$$c_i^{(\mathrm{i})}(t+\Delta t) = c_i^{(\mathrm{i})}(t) - \Delta t \sum_j \{H_{ij}^{(\mathrm{r})} + \kappa_{ij}^{(r)}(t+\Delta t)\} c_j^{(\mathrm{r})}(t+\Delta t) + \Delta t \sum_j \{H_{ij}^{(\mathrm{i})} + \kappa_{ij}^{(\mathrm{i})}(t+\Delta t)\} c_j^{(\mathrm{i})}(t). \tag{5.4b}$$

This fact becomes critical for modelling control of IVR using a laser pulse, where $\kappa_{ij}(t) = \mu_{ij}\,\mathscr{E}(t)$ is the product of the transition dipole matrix element and the pulsed field envelope $\mathscr{E}(t)$ (section 9).

6. Predicting IVR: specific examples

6.1. *1-propyne*

The first three acetylenic C–H stretching overtones and the combination band $\nu_1 + 2\nu_6$ all have been studied experimentally (Gambogi *et al.* 1993a, Go *et al.* 1993, McIlroy *et al.* 1994) and span the range from nearly complete localization to nearly full IVR in the low density of states limit. As such, they offer an excellent opportunity to compare with the predictions of our model.

SUR and Lanczos simulations were run with anharmonic overtone and combination bright states as starting points. The factorization model of section 4.2 in a diagonal anharmonic basis with different cubic coupling strengths and Born–Oppenheimer scaling parameters for each mode (figure 6.1) was used to calculate matrix elements. In such a basis, the spectral features appear at the correct energy, but show no fragmentation due to states carrying no oscillator strength. Some calculations were also done with matrix elements including the effects of kinetic and distance localization incorporated in the $c^{(2)}$ values. In all cases, we obtain semi-quantitative agreement with experiment by setting to 0.4 the average ratio of the cubic potential constants V_i to the diagonal anharmonicities of the anharmonic normal mode basis (Gambogi *et al.* 1993a, Go *et al.* 1993, McIlroy *et al.* 1994, Bigwood and Gruebele 1997). This factor would be close to unity in a harmonic normal mode basis.

The nearly isoenergetic $3\nu_1$ and $\nu_1 + 2\nu_6$ features are a particularly interesting case. The $P(t)$ from the spectra in figure 6.1 for both states exhibit a pattern of slowly decaying, deep quantum beats. Even without $c^{(2)}$ included, the long time decay rate of the pure overtone state is slightly faster than that of the combination band. This is a typical example of the competition between the lower connectivity of edge states and the lower couplings ($c^{(2)} < 1$) between interior states when there is significant kinetic or spatial localization. If connectivity in QNS alone without regard to matrix element size controlled the dynamics, the overtone should decay more slowly than the combination band. In the case of $3\nu_1$ and $\nu_1 + 2\nu_6$, the partitioning of energy into the methyl and acetylenic parts of the molecule is apparently sufficient to lower the rate of decay from the $\nu_1 + 2\nu_6$ feature even more, as seen in both experiment and calculation.

The effect is even more pronounced when a set of $c^{(2)}$ values is used which represents a lower bound on the possible values. The dilution factor of the $\nu_1 + 2\nu_6$ feature increases considerably toward unity, and little fragmentation on a 1–20 cm^{-1}

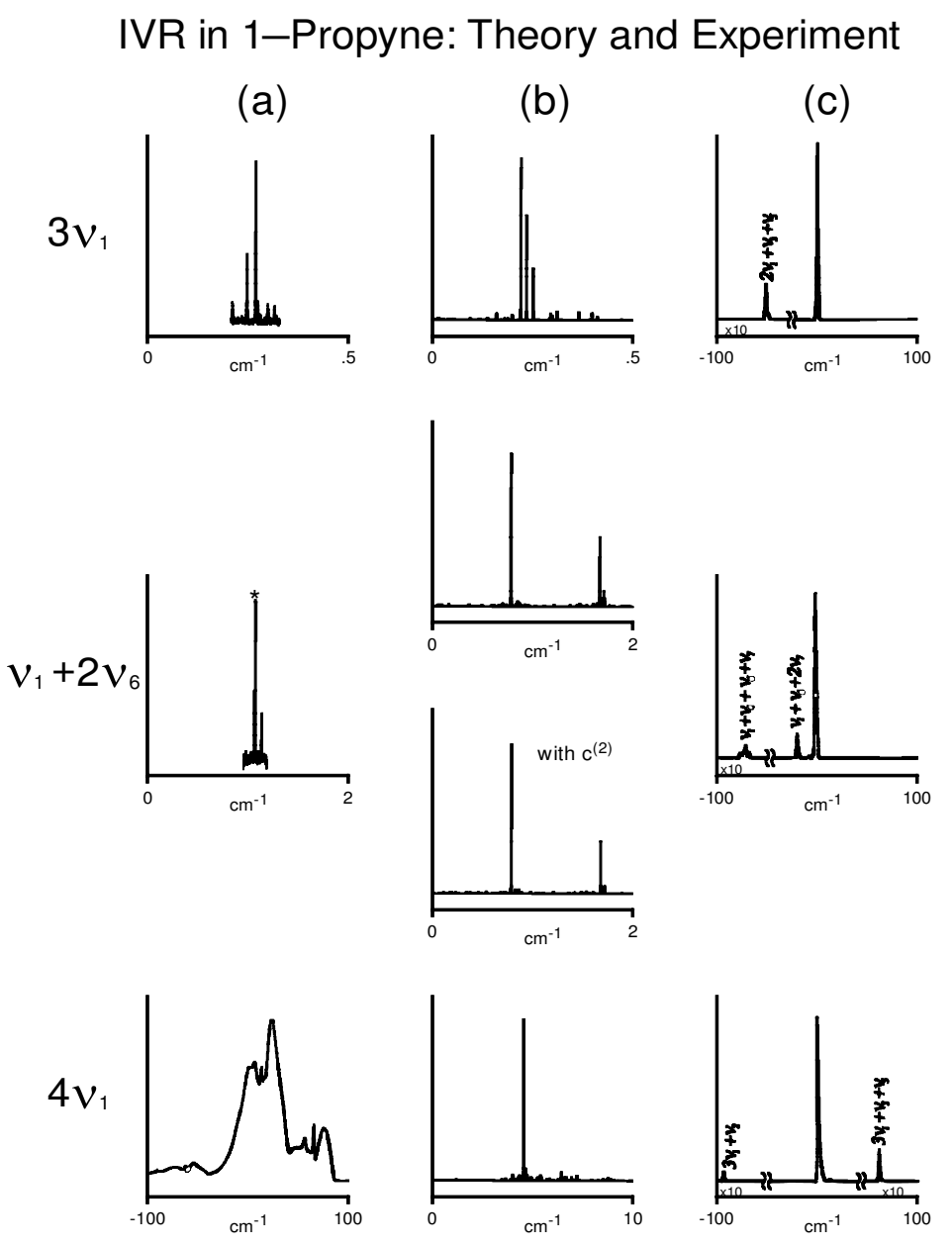

Figure 6.1. $3\nu_1$ (upper traces), $\nu_1 + 2\nu_6$ (middle traces) and $4\nu_1$ (lower traces) transitions of propyne as a function of excitation frequency from the feature centre. Column (a): experimental results (Crofton *et al.* 1988, Gambogi *et al.* 1993a, McIlroy *et al.* 1994). Column (b): detailed view of IVR computations with the factorized diagonal anharmonic Hamiltonian. Column (c): wider spectral overview of the same calculation with theoretical state assignments for the gateway states. For the combination band in the middle two traces, two calculations are shown: one without $c^{(2)}$, and one with the most conservative estimate of $c^{(2)}$ (all coefficients < 1), which shows a considerable smaller σ. Many of the small transitions disappear due to partial localization of the acetylenic and methyl CH stretching vibrations. Experiments have not covered the weaker feature predicted about 1 cm^{-1} from the largest peak.

scale is left, indicating that some of the couplings responsible for IVR in the calculation without $c^{(2)}$ bridged the methyl/acetylenic regions and were eliminated. However, a small transition a few cm^{-1} from the main peak is still predicted, but lies outside the experimentally scanned range.

It should be kept in mind that propyne is near the localization transition (Leitner and Wolynes 1996a). Our prediction that combination bands should decay faster than pure overtones based on low edge-state connectivity (Gruebele 1996c) is valid only when averaged over a large number of different states, and sufficiently above the threshold for IVR. At energies near the transition to delocalization, violations of this principle are not uncommon. In this still off-resonant regime, the precise location of the few gateway states is the key factor in determining the early decay characteristics, and propyne falls into this regime (Bigwood and Gruebele 1995b). At higher energies and for fully interior states (unlike $\nu_1 + 2\nu_6$, which is just off-edge) calculations for interior and edge states of propyne indeed show that interior states decay faster (Bigwood and Gruebele 1995b).

The third overtone shows evidence of strong off-resonant couplings dominating short time dynamics with a rapid initial drop to $P(t) \approx 0.5$, followed by a complicated pattern of quantum beats over a wide range of timescales. The simulations for the third overtone predict large off-resonant gateway peaks which are in agreement both in their assignments, and in their approximate positions from the central peak, with the experimental data (McIlroy *et al.* 1994). The relatively smaller simulated peak intensities indicate that the couplings to these levels are underestimated by the scaling model. The second overtone and adjacent combination band spectra also show small off-resonant gateway states. These are estimated by our calculation to be a factor of 50 less intense than the main band, and experimental data in the area of these wings are unavailable for comparison.

6.2. $SCCl_2$

Using the BSTR model, we have conducted numerous simulations of the thiophosgene molecule (Gruebele 1996c) to compare with experimental and *ab initio* results (section 8). Thiophosgene is particularly interesting because it allows one to look at heavy-atom IVR directly: its bright states, which include multiple combination bands of CS stretch, CCl stretch and bending modes are not unlike the interior states of XH overtone initiated IVR (section 8) in large molecules. The results are summarized in figure 6.2.

Figure 6.2(A) shows spectra and decays from the nominal C=S stretching overtone at 12000 cm^{-1} for two cubic coupling strengths (the first artificially low at the IVR threshold of $V = 0.2$ cm^{-1}, the second corresponding to the average molecular value of 2.5 cm^{-1}). The change from quantum beats to a smooth decay is evident, although even the smoothed lineshape does not appear exactly Lorentzian (*vide infra*).

Figure 6.2(B) presents the nearest neighbour level spacing statistics for excitation into an interior state near the 12000 cm^{-1} stretching overtone. It is important to note that even for couplings exceeding the actual molecular values, GOE statistics are not completely reached, although the dilution factor σ (Stewart and McDonald 1983) and participating phase space fraction F (Stechel and Heller 1984) in figure 6.2(C) approach values for nearly complete participation of the available levels. For F in particular, the difference in statistics between $F = 0.25$ and 0.3 can be significant, and an F as high as 0.2 and 0.27 does not generally go hand-in-hand with GOE statistics.

The bars on the dilution factors in figure 6.2(C) represent the second moment of many BSTR results with different constrained random distributions of n from

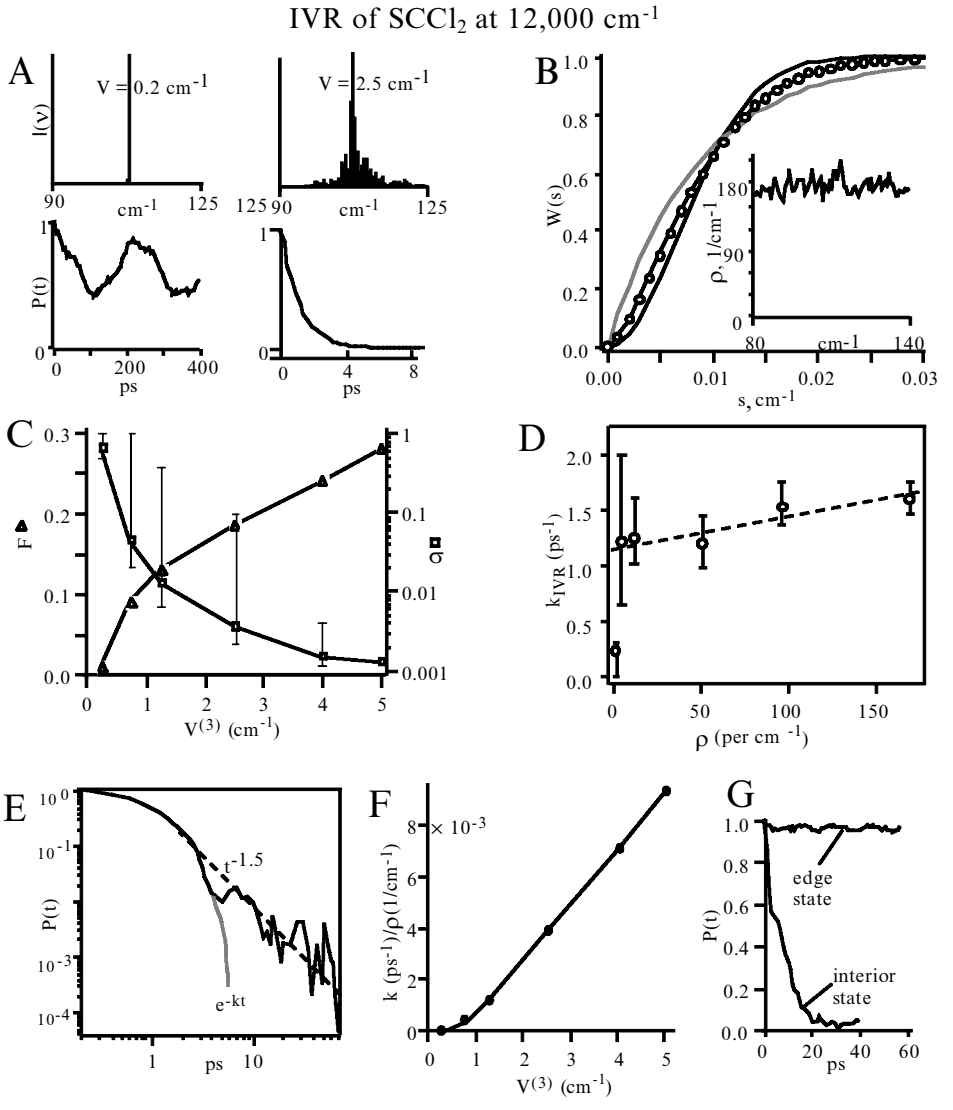

Figure 6.2. BSTR calculations for IVR in $SCCl_2$. The results in this figure illustrate the generic behaviour we find for heavy-atom IVR. (A) Spectrum and decay for a small (0.2 cm^{-1}) and a realistic (2.5 cm^{-1}) value of the average anharmonic coupling in a normal mode basis, showing transition from quantum beats to the smooth decay regime. (B) Level spacing statistics from the calculation (circles) compared to Poisson (dotted) and GOE (solid) results for $V = 2.5$ cm^{-1}; level statistics are always intermediate at realistic coupling strengths. (C) Heller's F and McDonald's σ values. The bars on σ indicate the spread of differently seeded BSTR calculations, indicating great sensitivity of the accessible phase space to $V^{(3)}$ at intermediate values. (D) The initial $(1/e)$ IVR rate k_{IVR} of $SCCl_2$ increases only very slowly once a critical density of states has been reached; there is no linear correlation between k_{IVR} and total density of states. (E) $P(t)$ is exponential at early times, and power law as $\approx t^{-3/2}$ in the transitional time before settling into a constant value. (F) The rate as a function of *anharmonic* cubic coupling $V^{(3)}$ shows a threshold ($k = 0$), superexchange ($k \sim V^{(3)4}$) and linear regime. As $V^{(3)}$ is increased further, there is presumably a final discontinuity as the entire phase space is explored and $P \sim t^{-5/2}$. (G) $P(t)$ for isoenergetic edge and interior states; the edge state has not achieved the threshold local density of connected states to undergo IVR.

equations (4.6) and (4.7). From the wide spread, one immediately concludes that the coupling strength and the total density of states alone are insufficient to describe the threshold for delocalization. In a regime of intermediate coupling strength or density of states, the *local* density of states coupled directly to the bright state must be known in order to predict IVR, and is subject to wide fluctuations between different molecules. We will return to this in section 7 in connection with the ρ dependence of dilution factor distributions averaged experimentally (Stewart and McDonald 1983) and theoretically (Bigwood and Gruebele 1997) over many molecules

The same threshold behaviour is evident in the early time dynamics, characterized by k_{IVR} rather than the dilution factor. Figure 6.2(D) shows the initial decay rate for groups of isoenergetic states as a function of the density of states. It rises rapidly near a threshold density $\rho_{\mathrm{th}} \approx 8\ \mathrm{cm}^{-1}$, then levels off and becomes essentially independent of the density of states. Whether the early or late time behaviour is used as a criterion, the ρ dependence of the extent of IVR shows threshold and saturation behaviour separated by a region of rapid change if the anharmonic coupling strength $V^{(3)}$ is held constant (section 7). This is quite incompatible with the idea that the IVR rate might depend quadratically on $V^{(3)}$ and linearly on ρ.

Figure 6.2(E) shows that $P(t)$ initially has curvature in a log–log plot, corresponding to an exponential decay (after the initial cos roll-off) as predicted by the Golden Rule using first-order perturbation theory. In the transitional regime however, $P(t)$ is linear on a log–log plot, in agreement with action-space renormalization models (Schofield and Wolynes 1993). At long times, $P(t)$ fluctuates about a constant value due to the maximum number of participating states. The power law decay at intermediate times indicates less efficient energy flow than predicted by the Golden Rule, and a non-Lorentzian lineshape (figure 1.2). In the case of $SCCl_2$ this is due to the triangle rule structure of the action space and exponential fall-off of matrix elements with n. It should be noted that the renormalization model predicts $P \sim t^{-5/2}$ *for* $\mathscr{N} = 6$ modes, while the calculated slope for interior states at 12000 cm^{-1} is 1.5, indicating incomplete access to the total phase space (Gruebele 1998).

This goes hand-in-hand with the dependence of k_{IVR} on energy. In terms of V_{rms}, k_{IVR} is a quadratic function following the region below threshold, where k_{IVR} is zero or ill defined. In terms of the cubic coupling strength $V^{(3)}$, the story is very different (figure 6.2(F)). Following the threshold region where $k_{\mathrm{IVR}} = 0$, the rate rises rapidly as $V^{(3)4}$ in the off-resonant regime, then becomes linear.

The $V^{(3)4}$ dependence can be rationalized in terms of off-resonant IVR (Bigwood and Gruebele 1995b): if the initial state couples to the long time manifold via an off-resonant state, two 'perturbation' steps are required (see also figure 7.3(*b*)). Essentially, the Golden Rule is replaced by a two-tier picture in which the first tier has only one or a few off-resonant states, and the second tier has a high density of states.

At stronger couplings V, the linear dependence is in agreement with analytical multi-tier models of IVR (Logan and Wolynes 1990). At even higher coupling strengths, one might expect k to become linear with a larger slope, and $P(t)$ to decay as $t^{-5/2}$ as the full phase space becomes accessible, unless QNS localization is somehow clamping the exponent (Gruebele 1998).

It should be noted that the transition from $V^{(3)4}$ to linear $V^{(3)}$ dependence occurs at a very low coupling strength ($< 1\ \mathrm{cm}^{-1}$), well below the actual value of the cubic anharmonicity of the molecule. In practice, IVR among heavy-atom modes in larger molecules will generally occur in a regime where cubic coupling $V^{(3)}$ and the Golden Rule coupling V_{rms} are not linearly related.

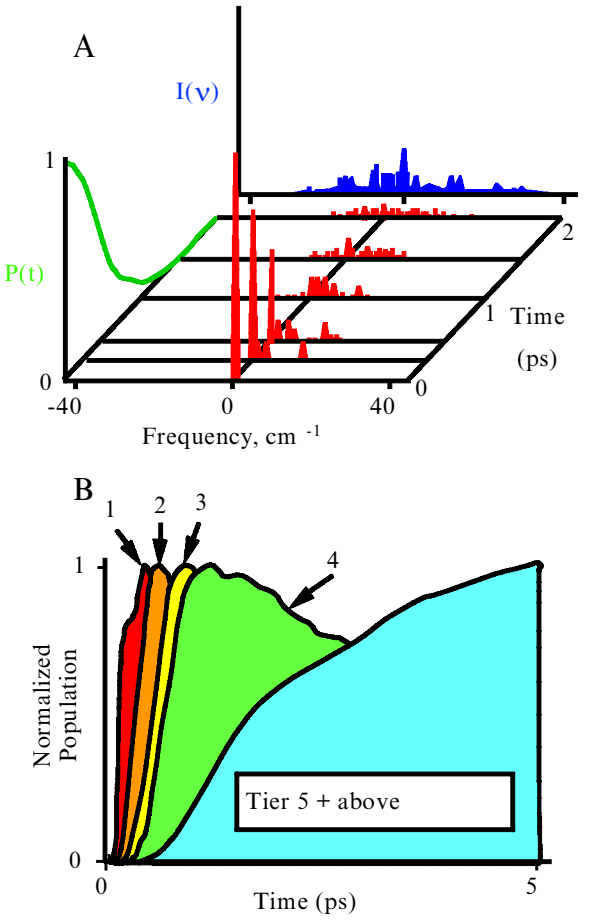

Figure 6.3. (A) $P(t)$ from the $v = 5$ CD stretching vibration, basis state amplitudes, and final spectrum of CDBrClF without an imposed tier structure. (B) When basis states are binned into tiers using equation (5.1), analysis of the calculation in (A) shows sequential flow, validating the idea of tiers. Since kinetic/distance localization are unlikely in CDBrClF, this would indicate extensive phase cancellation effects during IVR.

Finally, $SCCl_2$ also shows the typical behaviour for edge and interior states (figure 6.2(G)): on a given energy shell, interior states decay considerably faster than edge states in a compact molecule when kinetic and spatial isolation do not play a role.

6.3. *CDBrClF*

Figure 6.3 shows the results of simulations on the $v = 5$ CD anharmonic stretching bright state of CDBrClF with interlevel couplings calculated using the simplest scaling rule in equation (4.2). No tiers were assumed in the calculation, but levels were assigned to 'tiers' using the non-variational selection algorithm in equation 5.1. It should be emphasized that, unlike recent work in which tier assignments were made according to a specific third-order coupling term (Beil *et al.* 1997), our tier assignments are based on an effective mixing ratio $V_{vv'}/\Delta E_{vv'}$. This mixing ratio allows any order coupling (here $3 < n < 10$), provided the energy difference between the coupled levels is sufficiently small to allow mixing.

Figure 6.3(A) shows the $P(t)$ decay transient, the population of bright basis states as a function of time t, and the final spectrum. From this plot, it is clear that there exists a small subset of levels which are responsible for the initial amplitude transfer out of the bright state. Note that the initially populated basis states all lie to the blue of the bright state. If the off-diagonal coherences are included in the energy expectation value, energy is nonetheless conserved.

The time-dependent normalized population of levels assigned to each tier is shown in figure 6.3(B). The clearly sequential flow through the tier hierarchy is a validation of our method of assigning levels, and shows that a tier picture can indeed provide insight into the energy flow patterns even at high densities of states and for larger molecules.

6.4. *A simple model for methanol*

Rizzo and co-workers made the interesting observation that the $n\nu_{OH}$ and $(n-1)\,\nu_{OH}+\nu_{CH}$ stretching bands, which are strongly resonant for $n=5$, can show very different amounts of fragmentation even at resonance (Kuhn *et al.* 1997). They assign the more fragmented feature to a mixture with more OH-stretch character, based on integrated line strength and the fact that the OH stretch is the bright state. The less fragmented feature contains more of the CH bright state character. Two possible explanations are that there is a fundamental dynamical difference between the $\pm$ components of $|5\nu_{OH}\rangle \pm |4\nu_{OH}+\nu_{CH}\rangle$ at 50:50 mixing, or that chance coincidences with favourable distributions of dark gateway states account for the different fragmentation.

Using a simplified version of equation (3.3) for the C_{3v} rotor case, the corresponding off-diagonal matrix element scaling, and the BSTR model, we have calculated a statistical sample of possible IVR patterns for these two spectral features. The main parameters are given in (Bigwood and Gruebele 1997) and have been adapted here for a fourth-order coupling matrix element of 50 cm^{-1}. We find that for energy gaps ΔE_0 between the two zero-order states as small as 20% of the coupling strength, significant differences in fragmentation occur: 80% of the calculations show the mostly $|\nu_{OH}+\nu_{CH}\rangle$ feature to be more fragmented, while 20% show the mostly $|5\nu_{OH}\rangle$ feature to be more fragmented. For large ΔE_0, the approximately $|5\nu_{OH}\rangle$ feature is generally less fragmented, while for $\Delta E_0 = 0$, the fragmentation is more similar for the two features, although it still shows significant variation for different randomly seeded BSTR calculations. On the other hand, there seems to be no correlation between the relative sign of the two bright basis states and which feature is more fragmented. This makes sense based on first-order perturbation theory (which would be sign-independent), and seems to carry through even in a full calculation.

We conclude that dark state coupling variations can account for the observed results. This would imply that isotopic substitution of the oxygen or carbon atoms could lead to significant changes in fragmentation patterns.

7. IVR: general results

7.1. *Early, transitional and late times*

We now return to the question of timescales first discussed in section 1. Different experiments address different aspects of the IVR process. Some experiments measure the initial decay of the survival probability of a specified bright state (Lehmann *et al.* 1994). Other experiments measure the fraction of 'unrelaxed' wavefunction that remains after long times (Parmenter 1983). Only rarely have experiments and theory

explicitly considered the transitional timescale between these extremes (Felker and Zewail 1985, Kaufmann *et al.* 1989, Gruebele 1998). IVR can be subdivided into these three distinct timescales, characterized by very different phenomena (figure 1.1).

The earliest and historically the most commonly discussed IVR measure is the initial $P(t)$ decay of a spectral feature characterized by a lifetime τ, as $P(t)$ falls to a value of $1/e$, and the corresponding width of the spectral envelope. The local density of states and the specific couplings among states reasonably near the initial state in energy and quantum number govern the early dynamics. As a result, the initial rate of IVR and indeed whether a *particular* level will undergo IVR at all can be rather unpredictable without a detailed analysis, especially in small molecules of high symmetry (figure 6.2(G)).

At a much later time, the accessible action space of a molecule has been explored by the time-evolving bright state. The IVR packet has been distributed over bright basis states far away in quantum number, although the corresponding eigenstates essentially lie on the energy shell (depending on the width of the spectral feature and laser pulse duration). The accessible phase space is finite, and particularly in smaller molecules this manifests itself in a nonzero baseline value of $P(t)$ (Pechukas 1982). This end product of IVR, when the phases of eigenstates constituting the bright state are minimally correlated, has been described by F (Stechel and Heller 1984) and σ (Stewart and McDonald 1983).

At transitional times, molecules show novel behaviour connecting the early and late regimes (figure 6.2(E)). The dynamics depend on the coupling structure, such as off-resonant couplings from hydrogenic states or resonant heavy-atom couplings. However, at high local densities of states this coupling structure does not necessarily betray itself in terms of obvious quantum beats, but rather in terms of power law decays or a nonquadratic dependence on the intrinsic anharmonicity of the vibrational Hamiltonian (Schofield and Wolynes 1993, Gruebele 1998).

As discussed earlier, although the exact description of the anharmonicity is somewhat basis-set-dependent, the underlying nature of covalent molecular potential surfaces leads to similar scaling of the couplings in any reasonable bright state basis (normal, anharmonic, local mode). The local nature of IVR in the transitional regime even opens the possibility of controlling the IVR process (section 9) (Gruebele and Bigwood 1996).

7.2. *Localization*

A comprehensive understanding of localization phenomena is a prerequisite for any mechanistic exploration of IVR. This was first highlighted by Logan and Wolynes in 1990 in connection with Anderson localization (Logan and Wolynes 1990, Leitner and Wolynes 1996a). The physical effects leading to localization have already been discussed in examples in section 6. Here we summarize them and discuss them systematically:

(1) the rapid decrease in coupling size with quantum number difference between states (Parmenter 1983, Bigwood and Gruebele 1995b);
(2) directional action space 'bottlenecks' (e.g. triangle rule in equation (4.8)) (Gruebele 1996c);
(3) quantum mechanical interference effects due competing phases or signs of coupling matrix elements, particularly among off-resonant coupling chains (Gruebele 1996c, Pearman and Gruebele 1998a);

(4) edge location in action space (Gambogi *et al.* 1993b, Bigwood and Gruebele 1995b);
(5) kinetic or spatial isolation for states in the interior of action space (Freed and Nitzan 1980, Madsen *et al.* 1997);
(6) finite size of phase space (Pechukas 1982, Stewart and McDonald 1983).

Some of these (1, 6) are now well characterized, while the others are still under intensive experimental and theoretical study. These factors are also by no means independent from one another. The importance of localization cannot be overstressed, particularly in the transitional time regime, where the vibrational wavepacket is switching from local to global phase space exploration.

(1) Coupling size localization results from the rapid decrease in coupling matrix element magnitude with order n (Rashev 1990). The exponential decrease allows one to predict a maximum order $n_{\max}$ (quantum number difference between states) that will play a statistically significant role in IVR dynamics. As discussed in section 4, $n_{\max}$ depends on molecular energy, size, and the timescale of interest. In the limit of low energies and in small molecules, or at early times, $n_{\max}$ may be ≈ 4; in the limit of high energies, or at long times, $n_{\max}$ can exceed 6 and direct high-order couplings dominate (Pearman and Gruebele 1998a).

In the first limit, energy flow is more off-resonant: it proceeds via chains of low-order couplings off the energy shell (Stuchebrukhov and Marcus, 1993). Since IVR usually originates from features described by a small number of QNS cells, this has a dramatic impact on IVR at short to intermediate times. At short times, the accidental large or small size of couplings determines the initial rate k_{IVR}. At intermediate times, sequential flow limits the rate at which the vibrational energy can explore *new* parts of action space.

In the second limit, large jumps in quantum number on or near the energy shell are possible. In the QNS framework, resonant energy flow is confined within a (hyper)polyhedron of radius n. These can determine how much of the action space is eventually filled (Madsen *et al.* 1997, Pearman and Gruebele 1998a). In both limits, the drop-off of couplings with n places an upper bound on the local density of states that plays the major role in the threshold for IVR (equation (4.4) and Leitner and Wolynes (1996a)).

(2) Localization depends not just on the distance n in QNS, but also on direction correlations in QNS. The simplest of these is embodied in the vibrational triangle rule between triplets of n_{ij} in equation (4.8). Its effect is to impose a short range block-diagonal topology on the Hamiltonian matrix due to the redundancy of strong couplings. In the context of the QNS radius n polyhedra discussed above, the triangle rule introduces localization by ruling out some levels that would be included in the polyhedra by virtue of their radii alone.

This redundancy of couplings plays a role in the IVR dynamics during all phases of IVR. At short and intermediate times, the further reduction in the local density of states will result in somewhat higher IVR thresholds and slower rates. The most dramatic effect of the triangle rule is at long times. Here, the resultant barrier to exploration of large parts of the vibrational phase space will manifest itself in higher dilution factors (lower F ratios) and prevention of true ergodicity.

(3) Even when coupling chains are strong, states can remain unmixed. This more subtle localization effect is due to coherent cancellation between the multiple coupling channels that exist between almost all states in a realistic model Hamiltonian.

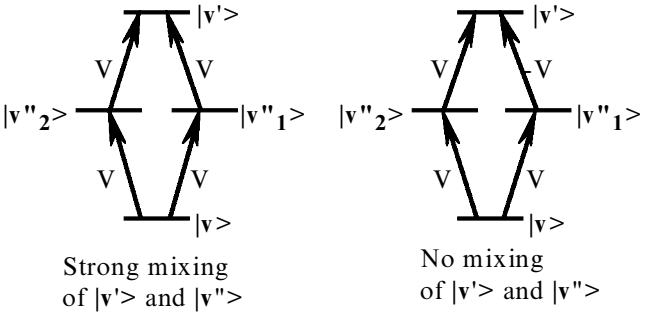

Figure 7.1. Extreme case of phase cancellation: on the left, states $|\mathbf{v}'\rangle$ and $|\mathbf{v}\rangle$ are strongly mixed, while on the right the eigenvectors of the lowest and highest energy eigenstates share no simultaneous $|\mathbf{v}'\rangle$ and $|\mathbf{v}\rangle$ components.

Although the effect of this on IVR is dramatic, it has received little explicit attention in the literature (Pearman and Gruebele 1998a). Figure 7.1 shows an example of phase cancellation for a four-level system. By merely changing the sign of one of the matrix elements between the intermediate and final levels, mixing can be completely eradicated. Couplings in real molecules vary in size, and phase cancellation is not quite in the random walk limit $V_{\text{eff}} \propto k^{1/2}V$, where k is the number of coupling chains. Nevertheless, interference is responsible for the observation in section 4 that phase cancellation abates the dominance of coupling chains, leading to a balance of direct high- and indirect low-order couplings in many cases. It can also be exploited in controlling IVR (Gruebele and Bigwood 1996).

(4) The local nature of couplings among feature (or bright basis) states illustrates most clearly the reason why edge states have higher IVR threshold energies and slower initial decays (on *average* and in the *absence* of kinetic or spatial localization of interior states in large molecules). This comes about simply because, by virtue of edge states' proximity to the QNS axes, many of their potential couplings would lead to unphysical negative quantum numbers in the remaining $2^{\mathcal{N}}$-tants of QNS. Their repertoire of potential coupling partners is limited by their location in action space (figure 6.2(G)).

(5) The local nature of molecular bonding and mass effects (Gambogi *et al.* 1993b, Perry *et al.* 1995, Madsen *et al.* 1997, Pearman and Gruebele 1998a) lead to localization among interior states with potentially many coupling partners (figure 3.2). Such localization can occur even, or especially, in very large molecules. Vibrational couplings between features tend to decrease exponentially with the number of bonds separating the atoms involved in the coupled vibrational motions (Pearman and Gruebele 1998a). A simple example was already mentioned above in equation (3.2): if energy E is deposited in a k-branched molecule, it may be partitioned into k branches with local energy E/k, lowering the effective energy available to IVR if the branches are independent from one another. As another example, a very heavy atom can separate a molecule kinetically into distinct regions, acting as a 'wall' which prevents access to the full QNS at long times.

Real molecules rarely fall into these limits, and moderate mass substitution or increases in the number of bonds do not necessarily decrease IVR rates (Lehmann *et al.* 1994). However, more subtle kinetic/distance localization does play a role, for instance in the extreme motion states of propyne (Gambogi *et al.* 1993b) discussed in section 6. Quantitatively, these effects are embodied in the $c^{(2)}$ coefficients discussed in section 4.

Very importantly, isolation localization implies size saturation of IVR. IVR thresholds and short times rates as a function of molecular size eventually level off due to the fact that the additional phase space associated with larger molecules is not initially accessible. This is the IVR version of functional groups in organic chemistry. 'IVR groups' are typically characterized by an exponential length scale of 1–2 bonds (Pearman and Gruebele 1998a). This makes them more extended than functional groups and certainly partially overlapping (except in the unlikely case of a molecule whose two halves are connected by a very heavy atom).

The isolation effect is strongest for linear molecules and weakest for aromatic ring compounds (Pearman and Gruebele 1998a). One can also imagine an extreme case where a chain can fold back on itself, and IVR is dominated by 'intermolecular' effects. Such cases may be important in the function of proteins and other macromolecules, but go beyond the scope of detailed discussion here.

(6) The finite extent of the available phase space causes equilibration at long times (Pechukas 1982). There is a direct analogy with standard first-order kinetics. Decays to a zero baseline result from irreversible processes. A finite equilibrium constant results in a finite baseline at long times. Similarly, a finite number N of accessible phase space cells (i.e. states) results in a final $P(t) \sim 1/N = \sigma$(Stewart and McDonald 1983). The finite size of action space in small molecules also results in 'reflections' of wave packet amplitude at the boundaries of QNS, as one source of quantum beats in addition to a sparse coupling structure.

All of these factors combine in any molecular system to make IVR a highly nonlinear process if thought of in terms of kinetic master equations (Gruebele 1998). Localization effects preclude a description of IVR with only averaged parameters such as ρ or V_{rms}. Examination of the problem in a bright state basis reveals that the fluctuations in the local density of states and coupling matrix elements are too severe to be averaged out. Correlations persist among the eigenstates with dramatic consequences.

One of the most interesting consequences of localization is the power law decay of $P(t)$ on the transitional timescale. This behaviour was first predicted by an analytical model using the state space formulation (Schofield and Wolynes 1993). In our calculations, all significant couplings were included, with no imposition of a particular topology. Our findings still show power law decays at intermediate times (e.g. figure 6.2(E)), although the behaviour can appear exponential at short times (Gruebele 1998).

As another consequence, the *average* behaviour of levels belonging to certain classes such as interior/edge states, and trends as a function of molecular size and shape can be predicted (Leitner and Wolynes 1996a, Pearman and Gruebele 1998a).

7.3. *Onset of IVR*

The onset of IVR requires that the energy spacing of locally accessible levels in QNS falls below a certain value characteristic of the coupling strength. Such states are necessarily coupled to the bright state through low-order (typically third or fourth) terms in the Hamiltonian. As a result, the accumulation of enough gateway bright basis states to permit the flow of vibrational energy out of a given feature depends on chance relationships between vibrational frequencies. This phenomenon is responsible for a wide statistical spread in the value of the dilution factor σ at intermediate state densities.

Figure 7.2(A) shows dilution factors derived from experiments performed over a

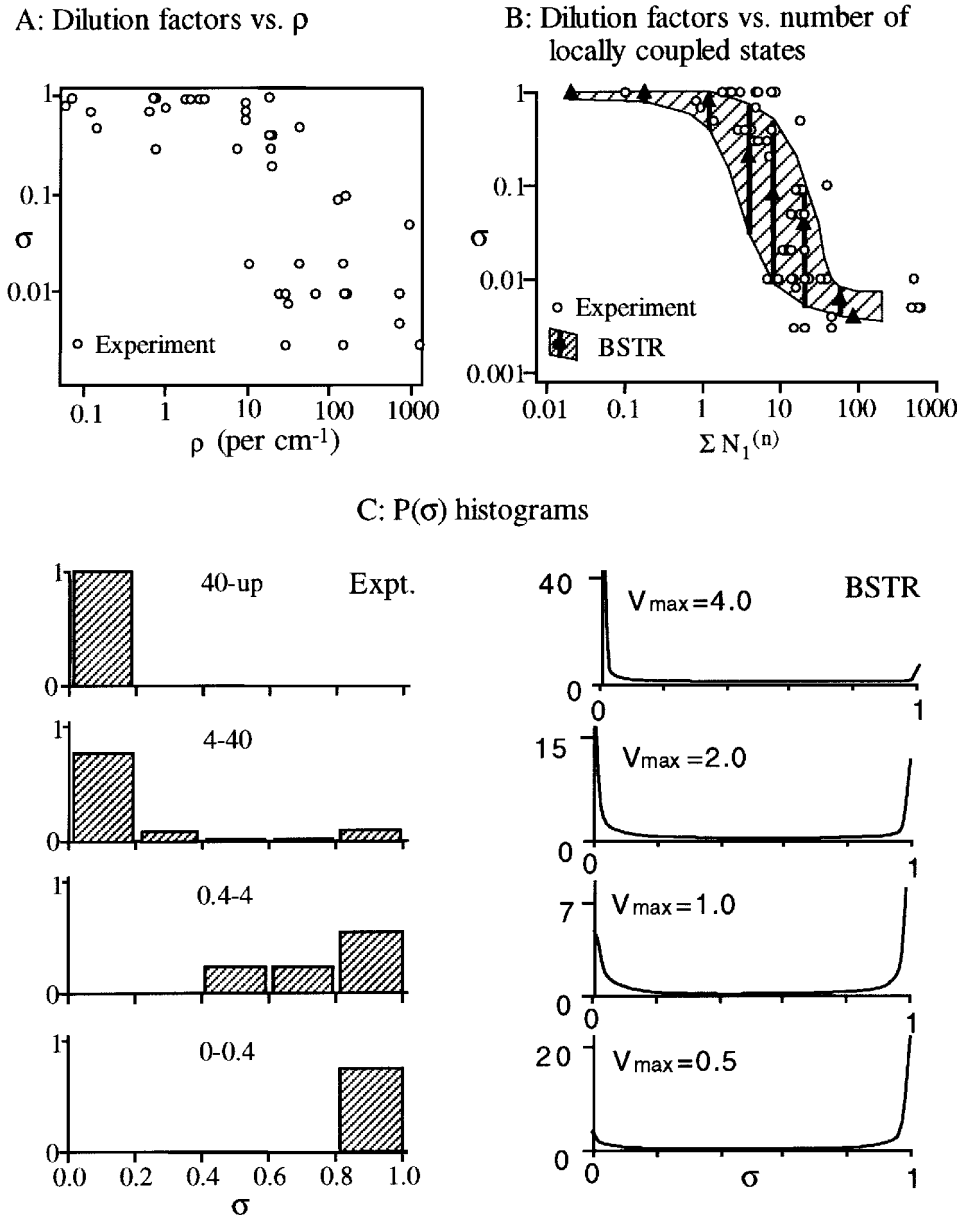

Figure 7.2. Dilution factor distributions. (A) Experimental (McDonald and co-workers) and calculated (BSTR) dilution factors for a number of organic molecules. There is a threshold density $\rho \approx 10$ cm^{-1} below which no significant dilution occurs, followed by a regime of large σ fluctuations, and a slower decrease in σ for very large molecules. The fluctuations are indicated by a bar for the BSTR calculations. (B) A plot of σ against the number of coupled states, which depends on the anharmonic coupling strength and *local* density of states, shows better correlation with experiment. (C) The experimental and BSTR distribution functions for σ are bimodal, indicating rapid onset of IVR when the anharmonic coupling strength exceeds a value dependent on the local distribution of bright basis states.

wide range of molecules and state densities (Stewart and McDonald 1983). Also plotted here are the results of BSTR calculations corresponding to the same range of organic molecules. The calculations show the same threshold and saturation behaviour as the experiment: $\sigma = 1$ at low state densities, followed by rapid fluctuations in the values at $\rho \approx 10$–$100\ \mathrm{cm}^{-1}$, followed by a slower decrease in σ as molecular size and ρ increase. The fluctuations at intermediate σ are due to the sensitivity of the local density of states on molecular parameters in this regime.

Based on the previous section, a more natural horizontal axis would be the effective number of directly coupled states $\sum N_1^{(n)}$, which increases much more slowly than exponentially with energy. This unitless quantity given by equation (4.5) takes into account the effects of the local density of states and coupling strength variations with order n. Figure 7.2(B) plots σ in terms of this quantity (evaluated approximately according to equation (4.5) with direct couplings only from Pearman and Gruebele (1998a) included). The transition to free IVR and full phase space access is more pronounced in this plot, while fluctuations in phase space access below the onset of strong IVR still exist. The transition to full IVR is centred about $\sum N_1^{(n)} \approx 1$–10.

Figure 7.2(C) shows the experimental distribution of σ values as a function of N_{coupled} derived by logarithmically binning figure 7.2(B) (i.e. $\sum N_1^{(n)} = 0.001$–0.010, 0.01–0.1, etc.). It also shows a calculated distribution of σ values for $SCCl_2$ by BSTR as a function of increasing coupling strength V (analogous to raising $\sum N^{(n)}$). The striking feature is the bimodal nature of the distributions: molecules either undergo IVR quite efficiently or not at all. From the lack of intermediate dilution factors, we can conclude that the delocalization transition for any given level is rapid and concerted as coupling strength increases, not unlike a phase transition in larger systems. The calculations are in good agreement with analytical forms initially proposed for the dilution factor distribution (Leitner and Wolynes 1996b).

Although these simulations show that the onset of IVR is sensitive to local properties, some general trends hold true. Edge states and extreme motion states tend to transition to IVR at higher energies and coupling strengths than their interior state counterparts. This is due to the localization effects described in the previous subsection. The same arguments can be made for the early delocalization of heavy-atom vibrations, with smaller energy gaps and more on-resonant energy flow.

7.4. *Off-resonant versus resonant and heavy-atom IVR*

A useful way of classifying vibrations into groups that exhibit similar IVR characteristics is on the basis of the energy separation between the bright state and its first-tier states. Figure 7.3 shows the range of cases, from off-resonant mixing, in which the main IVR gateway levels lie far from the IVR linewidth, to on-resonant mixing with gateway states within the IVR linewidth. Each of these mechanisms exhibit dramatically different behaviour, and propyne is an example of the first (section 6), while $SCCl_2$ above $8000\ \mathrm{cm}^{-1}$ is an example of the latter (section 8).

The question arises of how the initial IVR rate k_{IVR} scales in these different cases as a function of the cubic anharmonic coupling $V^{(3)}$, rather than as a function of the rms coupling V_{rms} (section 3). This is important because only $V^{(3)}$, not V_{rms}, provides a direct link between theory and the coarse features of the vibrational Hamiltonian on the one hand, and with experiment on the other hand.

Vibrational levels falling into the off-resonant class in general exhibit the quantum beats or near exponential decays traditionally associated with IVR. However, the mechanism in terms of bright state bases, which allow comparison of theory and

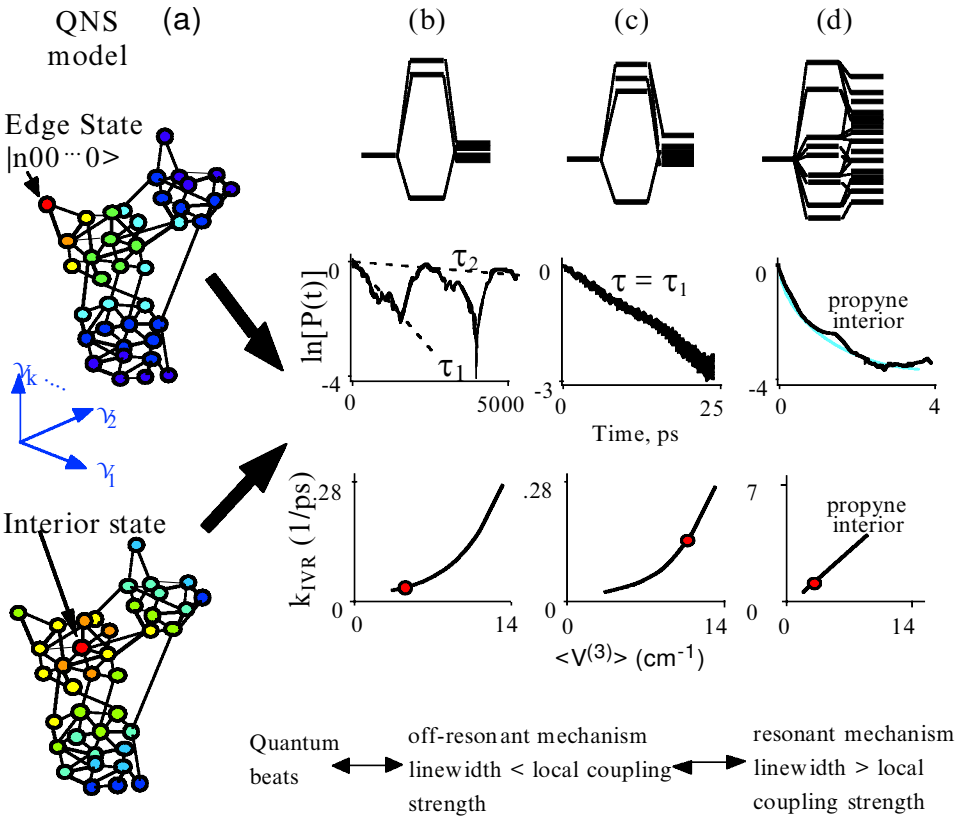

Figure 7.3. (*a*) Limiting IVR behaviour in the QNS picture. Cases from Bigwood and Gruebele (1995b). (*b*) Off-resonant, low density of states: below or near the IVR threshold quantum beats may have a rapid initial decay, but $\Psi(t)$ remains localized at long times and σ is large (example: propyne $3\nu_1$). (*c*) Off-resonant, higher density of states: smooth exponential decay and V^4 scaling of k_{IVR}. (*d*) On-resonant IVR with power law $P(t)$ and linear $k_{IVR} - V^{(3)}$ relationship (example: interior states of propyne near $3\nu_1$, $SCCl_2$ at longer times in figure 6.2).

experiment, differs from a single-step Golden Rule: it corresponds at least to a two-tier or off-resonant mechanism (Stuchebrukhov and Marcus 1993) with $k \sim V^4$ (Bigwood and Gruebele 1995b). The isolated gateway states may appear in the spectrum tens or hundreds of wavenumbers away from the main cluster of lines associated with the bright state, although they form a single feature together with the nominal bright state (figure 6.1). The decay patterns are generally dominated by quantum beats (e.g. $\nu_1 = 3$ in 1-propyne, figure 7.3(*b*)) or exponential decays (figure 7.3(*c*)).

IVR from levels with resonant gateway states tends to show more dramatic departures from 'naive' application of the Golden Rule. Although $k \sim \rho V_{rms}^2$ still holds approximately, the relationship between rate and *anharmonic* coupling becomes $k \sim V^{(3)}$. This change in rate-coupling relationships follows from the behaviour of the local density of states in analytical Caley tree models in the appropriate limit (Logan and Wolynes 1990, Leitner and Wolynes 1996a, b). In addition, decay transients in the transitional time window are generally better described by power laws than by exponentials (figure 6.2(E)). A rate in the exponential sense cannot even be defined (section 1).

Edge states and light-atom motions such as the hydrogenic stretching overtones, which with a few noteable exceptions (Smalley 1982, Felker and Zewail 1985, Geers *et al.* 1994) represent nearly all of the experimental date for $P(t)$, fall almost exclusively into the off-resonant regime due to their lower local densities of states as discussed above. As such, they are more likely to show a $k \sim V^m$ dependence with $m > 1$ for the anharmonic coupling strength V, not just for V_{rms}. However, these states represent only a small fraction of the total number of available vibrational levels of organic molecules, even if only features with reasonable oscillator strength are counted.

Interior states and heavy-atom vibrations with their higher local densities of states represent the overwhelming number of vibrational features. They most often fall into the resonant regime, for which the QNS picture is more representative as a zero-order approximation. Because they represent an overwhelming number of vibrational states, they could arguably be said to represent generic IVR. Moreover, IVR at long times involves the transport of vibrational energy across the heavy-atom molecular backbone. Thus, all IVR, regardless of the initial state, progresses via resonant mechanisms at intermediate to long times (see also section 4 on direct couplings versus chains at small ΔE_0). We address this experimentally in the next section.

8. An experiment: $SCCl_2$

At intermediate times IVR in nearly all molecules is governed by 'heavy-atom' motions, regardless of the nature of the initially prepared state. During this phase of IVR the degree of randomization, which is critical to the RRKM theory of reaction rates, is determined by the ability of the molecular backbone to transfer vibrational energy.

Most experiments look at IVR initiated in hydrogenic stretching modes. The IVR of the backbone manifests itself only indirectly in the fragmentation of the bright state. Further fragmentation of the dark states and their coupling patterns are not easily accessible in such experiments. A notable recent exception are vibration–rotation double resonance experiments, which can probe the IVR properties of dark states (Lee and Pate 1997).

Our approach is designed to look directly at backbone modes: we simply eliminate all hydrogen atoms from the molecule to obtain a molecular model for pure backbone IVR. As all ground state vibrations of thiophosgene ($SCCl_2$) involve second- and third-row atom motions, and four are Franck–Condon active from the $\tilde{A}$ and $\tilde{B}$ states, this small molecule is an ideal benchmark for direct experimental studies of the mechanisms that govern resonant IVR and the transitional timescale. We describe frequency domain experiments using dispersed fluorescence (DF) and stimulated emission pumping (SEP) under collision-free conditions in a molecular beam to explore IVR in $SCCl_2$, and to test the predictions of our theoretical models (Bigwood *et al.* 1998).

Figure 8.1 shows SEP experiments at 3680 and 9700 cm^{-1} above the vibrational zero point energy. Dispersed fluorescence spectra shows a sudden increase in the number of transitions at the 20 cm^{-1} resolution level about 8000 cm^{-1}, indicating fragmentation on a > 20 cm^{-1} scale. The SEP spectra (0.2 cm^{-1} resolution) reveal even finer structure: above 8000 cm^{-1}, bright states assignable to nominal normal mode states are fragmented to varying degrees on the energy shell.

The low-resolution DF data were directly fitted (with < 1.5 times the experimental uncertainty) to a 6D fully anharmonic curvilinear surface (MPG2, Bigwood *et al.* (1998)). To enhance convergence, this surface was initially pre-fitted to 1000 Monte

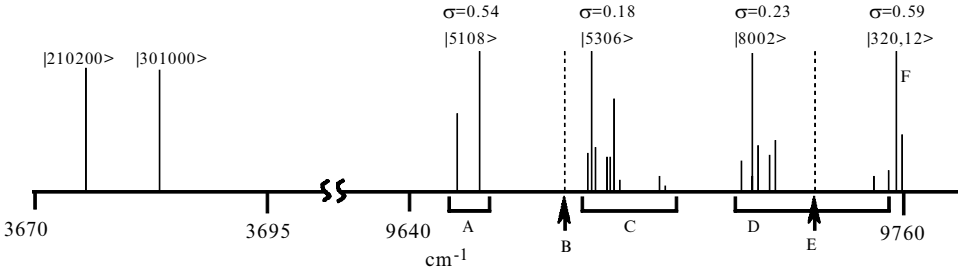

Figure 8.1. Vibrational features as measured by 0.2 cm^{-1} resolution SEP experiments. In the examples shown here, $SCCl_2$ is pumped from the vibrational ground state to the region of the 1^2 or 2^14^2 $\tilde{B}$ state vibrational levels ('dump states'), then back down to the ground state energies shown. Rotational contours have been deconvoluted, and individual transitions assigned to $|v_1, v_2, v_3, v_4\rangle$ features by comparing relative intensity changes from different dump states. Higher resolution SEP scans to the right of the fluorescence ladders reveal weak localized anharmonic interactions at low energy and resonant IVR at high energies. All features are normalized to the same maximum intensity; arrows and dashed lines indicate apparently unfragmented transitions with $\sigma = 1$. Even at the 0.2 cm^{-1} resolution level, large fluctuations in σ on the energy shell at 9700 cm^{-1} are evident, indicating transition towards free energy flow among heavy-atom modes.

Carlo sampled four-pair GVB correlated *ab initio* points to assure inclusion of reasonable terms in the PES up to 22000 cm^{-1} (Madsen *et al.* 1997). One interesting question concerns the predictivity of the Hamiltonian derived from low-resolution data for the high-resolution data. Fragmentation patterns similar to the SEP experiments at 9700 cm^{-1} are indeed predicted using SUR (section 5) and the DF-fitted experimentally derived potential surface (Bigwood *et al.* 1998). This indicates that the coarse anharmonic level structure (feature structure) of the Hamiltonian does constrain IVR on all timescales, possibly down to the eigenstate level. The < 20 cm^{-1} energy scale structure of the fragmented features at 9600 cm^{-1} is mostly resonant in terms of couplings of a normal coordinate Hamiltonian derived from the curvilinear DF-fitted PES, and can be assigned to resonant gateway states. Analysis of the coupling structure shows that IVR on all energy scales has a significant on-resonant component for heavy-atom vibrations.

Scanning the energy from the zero point to > 15000 cm^{-1} allows one to scan the total density of A_1 symmetry states from 0.02 cm^{-1} to 200 cm^{-1}. At the same time, the local density of states scans to > 1 cm^{-1}, roughly the density of gateway states observed in the spectrum for clumps at high energy. The behaviour of the features closely mimics figure 7.2. At low energy they correspond to a single eigenstate, such as the $|210200\rangle$ state at the bottom of figure 8.1. At high energies, fragmentation becomes very sensitive to the coupling structure: unfragmented (dashed) features are interspersed with highly fragmented features (e.g. point B on figure 8.1). The observed pattern is compatible with the large fluctuations predicted for the dilution factor at the transition to free energy flow, and with a bimodal distribution.

A detailed analysis of the experimentally derived Hamiltonian will show whether $k \sim V^{(3)}$ and if nonexponential $P(t)$ occur at higher energies. $SCCl_2$ should become an ideal system for studying IVR among heavy-atom vibrations from the sparse to nearly irreversible regime.

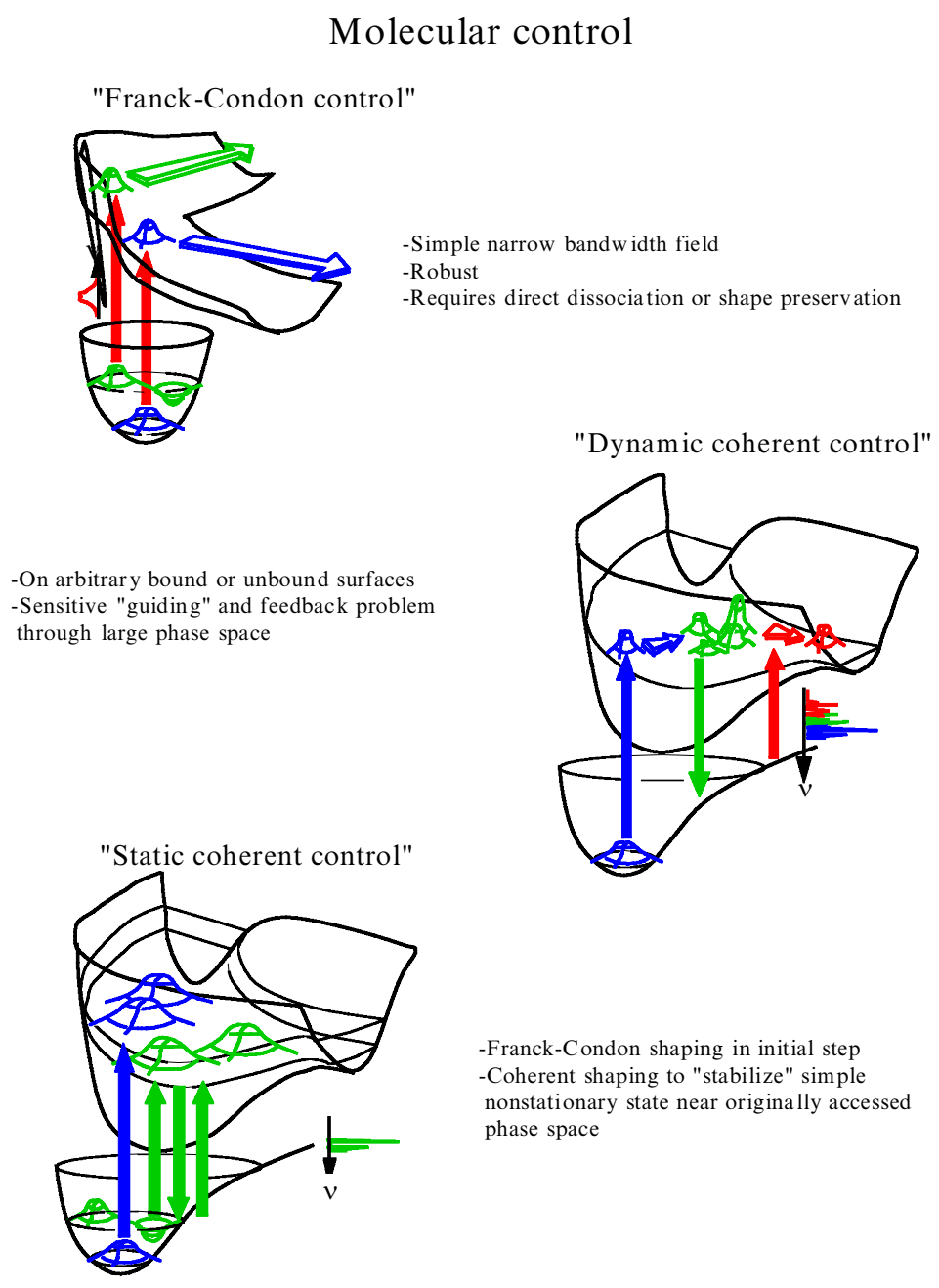

Figure 9.1. Approaches to molecular control. Upper diagram: Franck–Condon control uses a preparation pulse to shape the dissociative wavepacket and place it on different regions of the potential to obtain specific reactivity. Middle diagram: dynamic coherent control uses quantum interference via a set of intermediate states (not shown) or by cycling amplitude between several surfaces. Lower diagram: our proposed static coherent control combines Franck–Condon pre-shaping (green and blue features) with coherent cycling and phase chirping to freeze the polyatomic molecular phase space into a lower-dimensional manifold.

9. Coherent freezing of IVR

9.1. *Motivation*

Two successful frameworks for controlling unimolecular reactivity have emerged during the last decade. One uses quantum coherence to control reaction dynamics (Brumer and Shapiro 1989, Kosloff *et al.* 1989, Warren *et al.* 1993, Krause *et al.* 1995). The other involves Franck–Condon control, usually on a rapidly dissociative surface (Bronikowski *et al.* 1991, Crim 1993). They are illustrated in figure 9.1.

The idea of Franck–Condon control is to shape the reactive wave packet by pumping it from different intermediate states (figure 9.1, top). Differently shaped wave packets are launched with different momenta, and may concentrate in one of several reaction channels. An important restriction is that dissociation must either be direct, or memory of the induced shape must be retained in some other fashion during reaction. The idea has been successful with several small polyatomic molecules (Bronikowski *et al.* 1991, Crim 1993).

Dynamic coherent control is more general because the wavepacket can be optically modified during the reaction process, limited only by the structure of the available eigenstates. The shape of the reactive wavepacket can be controlled by quantum interference through either a set of intermediate states (Brumer and Shapiro 1989), or by coherent cycling between several sets of states (e.g. on two surfaces, figure 9.1, middle) (Kosloff *et al.* 1989, Scherer *et al.* 1991). This then becomes a guidance and feedback problem (Warren *et al.* 1993). Experimentally, coherent control has been achieved in systems with one or two heavy atoms (Park *et al.* 1991, Warren *et al.* 1993).

IVR poses a challenge to both approaches when applied to multidimensional bound surfaces of polyatomic molecules (>2 second or higher row atoms). It destroys memory of wavepacket shape through dephasing, which directly negates the first approach. It complicates the second approach: the guidance problem can be solved in principle by feedback, no matter how complex the structure of the underlying eigenstates, but impractical fields and amounts of feedback information may be required to guide the wavepacket far away in phase space from its initial location. This is exacerbated by the fact that most current experiments read out only a few highly averaged feedback parameters, in effect providing a very small and fuzzy window on wavepacket motion.

In a trivial sense, IVR simply sets values for the eigenstate transition moments and energies through the presence of features. In practice however, the knowledge gained by a careful analysis of IVR (sections 1–8) provides much guidance to design a robust control experiment, much in the sense that a bridge engineer would use guiding principles to construct an embankment, rather than to use feedback in the form of collapsed embankments to improve design.

Figure 9.1 (bottom) proposes a scheme we call 'static' coherent control, which combines features of Franck–Condon and coherent control to effect selective reactions in polyatomic molecules (Gruebele and Bigwood 1996). Rather than guiding the wavepacket far away in phase space, the goal is to control reactivity by 'freezing' it in place, that is, by turning off IVR. This switches the timescales of dissociation of an activated bond (often slow) and IVR from that bond (often fast). Selectivity is achieved in two steps: a specifically shaped bright (pre)dissociating state is excited on a (pre)dissociative surface; IVR is then frozen by a coherent laser pulse.

The first 'Franck–Condon' step sets up selective reactivity: feature states or resonances have simple nodal structures following excitation, and couple to reactive

continuum channels in specific non-statistical ways. This specificity is usually lost before dissociation occurs due to phase decorrelation of the feature by IVR. The second 'coherent' step maintains specificity by 'freezing in' the initial wavepacket shape, i.e. by slowing down the IVR process. The problem of slowing down dephasing is simpler and more robust than the general control problem because the goal is merely to maintain the wavepacket in a known part of phase space.

The second step is possible because the system evolves under a joint molecule–laser Hamiltonian during excitation; coherent cycling and chirped excitation of different eigenstates under a feature can maintain the initial simple nodal structure of a feature for $t > 1/k_{\mathrm{IVR}}$. In effect, coherent control reduces the molecular projection of the total Hamiltonian to a low-dimensional system where Franck–Condon control is effective, by increasing the dephasing timescale beyond the dissociation timescale even in the presence of a bound potential well.

The key to this second step is the slower than exponential IVR among the skeletal vibrational modes. Power law decays $P(t) \sim t^{-\delta/2}$ with exponents δ of the order of 2–4 are generic features of IVR experiments (Kaufmann *et al.* 1989, Gruebele 1998) and simulations (Gruebele 1996c, 1998). The number of control parameters is roughly $2/P(t)$ because there is a phase and an amplitude to be controlled for every participating state. If decays were exponential, the number of control parameters would grow exponentially with time, but instead it just grows as a polynomial.

In keeping with the main topic of this review, we now address the problem of coherently slowing the dephasing process in a manner that maintains the initial feature state (Gruebele and Bigwood 1996). We will discuss the specific example of $SCCl_2$. It should be emphasized that either maintaining population in the upper state by continuously pumping, or by exciting a narrow bandwidth to obtain a near-stationary state, are not helpful because the resulting states have an eigenstate-like quasi-random nodal structure. Coherent control works by freezing the molecular wavepacket in the reactive manifold into its initial simple nodal structure for a sufficiently long time.

9.2. *Freezing IVR in $SCCl_2$*

With the objective of stemming vibrational dephasing for a time long enough to observe selective chemistry, we have developed a numerical model for the determination of optimal laser pulses to be used as the starting point for IVR control experiments. Here, we briefly discuss the molecule-radiation Hamiltonian, electric field representation, and optimization procedure.

In the semiclassical field representation, the Hamiltonian becomes

$$H = H_{\mathrm{mol}} + H_{\mathrm{int}}(t). \tag{9.1}$$

For the molecular Hamiltonian, we use the factorization model for $SCCl_2$ from sections 4 and 6 (figure 4.1) (Madsen *et al.* 1997). This performs exceedingly well at predicting the positions and coupling strengths of the first few gateway states, which are by far the most important in controlling IVR at short times. To this, we add a single level $|0\rangle$ to represent the initial state manifold. (Even more flexible control is possible with more levels.) The target for freezing is the time-independent bright state $|i\rangle$, which carries all the oscillator strength. It then follows that $\langle i|H_{\mathrm{int}}|0\rangle = \langle i|\mu|0\rangle \cdot \boldsymbol{E}(t)$ represents the coupling by the electric field. In practice, we prediagonalize H_{mol} using equation (5.2) so that H takes on a Golden Rule form, except that the couplings are now time-dependent and couple the ground state $|0\rangle$ to the prediagonalized upper state manifold over which the oscillator strength of $|i\rangle$ has been

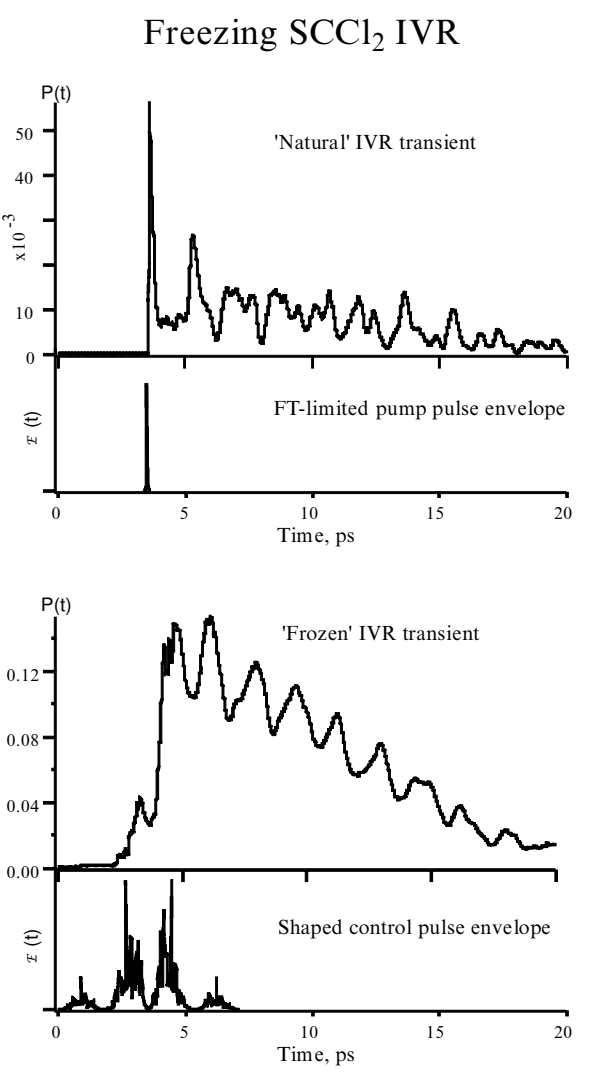

Figure 9.2. SUR calculation of coherent manipulation of IVR in the $v_1 = 8$ state of $SCCl_2$ using a factorized Hamiltonian. Upper diagram: using Fourier-transform-limited 0.5 mJ 80 fs Gaussian pulse. Lower diagram: using same pulse shaped by a 64-element phase and amplitude modulator. The pulse has a simple amplitude and phase structure and narrow bandwidth, yet freezes the feature in place for 100 times longer than the transform-limited pulse. Note that the pulse duration is shorter than the freezing time, and that constraints in the calculation ensure that the target is a coherent single-feature wave packet, and not a continuously replenished incoherent upper state population.

distributed. This form of H is ideally suited for propagation by equation (5.4) which implements nonperturbative propagation in the strong-field limit.

The electric field is represented in a Daubechies wavelet basis. In addition to the computational speed, wavelets provide a nearly physical representation of the discrete phase and amplitude channels of available experimental (Kawashima *et al.* 1995, Dugan *et al.* 1997) pulse shaping systems. By physically modelling the input pulse, pulse dispersion and the pulse control mask, the laser pulses are kept in the realm of what can be achieved in the laboratory. The total input bandwidth is constrained by

a ± 300 cm^{-1} wide Gaussian envelope, and the pulse area is not allowed to exceed a reasonable maximum value.

The maximum time step in the SUR algorithm is limited by the total bandwidth of the system. For efficiency, we make the rotating wave approximation, subtracting off the central frequency from the laser field, and from the energy difference between the ground and bright states. This approximation is valid for resonant laser pulses with intensities that are typical of our laser system.

The optimization is performed by simulated annealing to avoid trapping in one of many possible local minima. Ideally, one would like the evolving state $\Psi(t)$ to remain perfectly localized at $|i\rangle$, with the survival probability, $P(t) = |\langle \Psi(t)|i\rangle|^2$, unity at all times. We therefore choose the integrated survival probability,

$$W = \int_0^{t_{max}} P(t)\,\mathrm{d}t \tag{9.2}$$

as the function to be optimized to a desired time t_{max}. Requiring not just the *final* state at $t = t_{max}$ to be near $|i\rangle$ makes the solution less optimal but more robust since the wavepacket is prevented from escaping the initial region of phase space at intermediate times.

As discussed in the last section 9.1, several trivial cases must be avoided. A pulse shape which maximizes equation (8.2) by efficiently pumping a large population into the target wavefunction at short times without slowing the decay rate is of no help in creating long-lived bright state wavepackets for selective chemistry experiments. Normalizing W by $(1 - P_{gnd})$, the population remaining in the ground state at long times, addresses this issue. Another uninteresting result is obtained when the laser bandwidth is reduced to the point of pumping a few closely spaced eigenstates, since a single eigenstate of course has a small but constant overlap with $|i\rangle$. Calculating $P(t)$ by projecting onto the eigenstate spectrum of the bright state $|i\rangle$, in conjunction with the above normalization by $(1 - P_{gnd})$ eliminates this possibility.

Figure 9.2 presents the results of an optimization of IVR in thiophosgene $v_1 = 8$. When pumped with a Fourier-transform-limited Gaussian pulse, the 'natural' IVR proceeds with a rapid initial decay, followed by a series of small quantum beats. Pumped by an optimized pulse, the initial fast decay is slowed by nearly two orders of magnitude. This calculation was done using only 64 control channels, and results in a relatively smooth electric field envelope. Sensitivity to small changes in the field is quite low, as evidenced by a rapid approach to convergence as the coarse field structure in the four-lobed pulse appears. This is what one should expect from a tier picture, as most of the decay arrest occurs by manipulating coherent cycling between the ground, bright, and the few gateway states with direct couplings to the bright state. It should be noted that the 5 ps duration of the control pulse is still noticeably shorter than the lengthened $P(t)$.

We believe that this type of IVR coherent control, coupled with exploitation of Franck–Condon effects, can provide a simple and robust route to polyatomic molecular control.

10. Conclusions

The following are the messages we hope the reader will take away from this summary of recent developments.

(1) In the feature to eigenstate hierarchy, features occupy an equally important position; features are remnants of the uncoupled Hamiltonian which organize spectra due to the small ratio of anharmonic terms $V^{(3)} a^{n-3}$ to harmonic terms ω in the molecular Hamiltonian.

(2) The vast majority of IVR in the intermediate time regime proceeds via the heavy-atom backbone. The resulting slower than exponential dephasing in the intermediate regime provides a handle for coherently controlling the IVR process.

(3) Localization in various guises plays a dominant role in IVR, and its effects are best seen in bright state or feature bases, which emphasize the simple wavefunction patterns ultimately responsible for localization. Localization plays a role at transitional and late times, and goes well beyond the appearance of quantum beats and similar well studied phenomena in sparse systems.

(4) Heavy-atom participation, interior location of a state in QNS, and importance of direct couplings at a high *local* density of states predispose IVR to occur via on-resonant mechanisms. The initial rate k_{IVR} is then related linearly to anharmonic couplings among features of the Hamiltonian; decay at longer times is not characterized by a rate at all, but rather by a power law with an exponent depending on the size of the accessible phase space; the ultimate dispersion $1/\sigma$ of the wave packet through state space is much greater.

Acknowledgements

We wish to thank R. Pearman and D. Madsen for their contributions on potential factorization and direct versus indirect couplings, and M. Davis, M. Kellman, D. Leitner, N. Sibert, P. Wolynes and R. Wyatt for helpful discussions. Funding was provided by the National Science Foundation, and M.G. held Sloan and David and Lucile Packard Fellowships while this work was carried out.

References

Abramson, E., Field, R. W., *et al.*, 1984, *J. chem. Phys.*, **80**, 2298.
Beil, A., Luckhaus, D., *et al.*, 1997, *Ber. Bunsenges. Phys. Chem.*, **100**, 1853.
Bentley, J. A., Brunet, J. P., *et al.*, 1989, *Chem. phys. Lett.*, **161**, 393.
Bigwood, R. and Gruebele, M., 1995a, *Chem. phys. Lett.*, **233**, 383; 1995b, *Chem. phys. Lett.*, **235**, 604; 1997, *ACH Models in Chemistry* **134**, in the press.
Bigwood, R., Milam, B., *et al.*, 1998, *Chem. phys. Lett.*, in the press.
Bixon, M. and Jortner, J., 1968, *J. chem. Phys.*, **48**, 715.
Bondybey, V. E., 1984, *Ann. Rev. phys. Chem.*, **35**, 591.
Brody, T. A., Flores, J., *et al.*, 1981, *Rev. mod. Phys.*, **53**, 385.
Bronikowski, M. J., Simpson, W. R., *et al.*, 1991, *J. chem. Phys.*, **95**, 8647.
Brumer, P. and Shapiro, M., 1989, *Acc. Chem. Res.*, **22**, 407.
Bullock, W. J., Adams, D. K., and Lawrance, W. D., 1990, *J. chem. Phys.*, **93**, 3085.
Bunker, D. L., 1962, *J. chem. Phys.*, **37**, 393.
Burleigh, D. C., McCoy, A. B., *et al.*, 1996, *J. chem. Phys.*, **104**, 480.
Chuang, M. C., Baggott, J. E., *et al.*, 1983, *Faraday Discuss. Chem. Soc.*, **75**, 301.
Crim, F. F., 1993, *Ann. Rev. phys. Chem.*, **44**, 397.
Crofton, M. W., Stevens, C. G., *et al.*, 1988, *J. chem. Phys.*, **89**, 7100.
Cullum, J. K. and Willoughby, R. A., 1985, *Lanczos Algorithms for Large Symmetric Eigenvalue Computations* (Boston: Birkhauser).
Davis, M. J., 1993, *J. chem. Phys.*, **98**, 2614; 1995, *Int. Rev. phys. Chem.*, **14**, 15.
Dugan, M. A., Tull, J. X., *et al.*, 1997, *J. Opt. Soc. Am.* B, **14**, 2348.
Ezra, G. S., Martens, C. C. *et al.*, 1987, *J. phys. Chem.*, **91**, 3721.
Feit, M. D., Fleck, J. A., *et al.*, 1982, *J. comput. Phys.*, **47**, 412.

Felker, P. M. and Zewail, A. H., 1985, *J. chem. Phys.*, **82**, 2961, 2975.
Fleming, G. R., 1986, *Chemical Applications of Ultrafast Spectroscopy* (Oxford: Oxford University Press).
Founargiotakis, M., Farantos, S. C., *et al.*, 1989, *J. chem. Phys.*, **91**, 1389.
Freed, K. F., 1976a, *Topics appl. Phys.*, **15**, 23; 1976b, *Chem. phys. Lett.*, **42**, 600.
Freed, K. F. and Gelbart, W. M., 1971, *Chem. phys. Lett.*, **10**, 187.
Freed, K. F. and Nitzan, A., 1980, *J. chem. Phys.*, **73**, 4765.
Fried, L. E. and Ezra, G. S., 1987, *J. chem. Phys.*, **86**, 6720.
Friesner, R. E., Bentley, J. A., *et al.*, 1993, *J. chem. Phys.*, **99**, 324.
Gambogi, J. E., Kerstel, E. R. T., *et al.*, 1993a, *J. chem. Phys.*, **100**, 2612.
Gambogi, J. E., Timmermans, J. H., *et al.*, 1993b, *J. chem. Phys.*, **99**, 9314.
Geers, A., Kappert, J., *et al.*, 1994, *J. chem. Phys.*, **101**, 3618.
Georges, R., Delon, A., *et al.* 1995, *J. chem. Phys.*, **103**, 1732.
Go, J., Cronin, T. J., *et al.*, 1993, *Chem. phys.*, **175**, 127.
Gray, S. K. and Verosky, J. M., 1994, *J. chem. Phys.*, **100**, 5011.
Gruebele, M., 1996a, *J. chem. Phys.*, **104**, 2453; 1996b, *J. phys. Chem.*, **100**, 12178; 1996c, *J. phys. Chem.*, **100**, 12183; 1998, *Proc Natl Acad, Sci.* USA (in the press).
Gruebele, M. and Bigwood, R., 1996, *Mechanisms and Control of Molecular Vibrational Energy Redistribution* SECAMP, October 1996 (Southern European Conference on Atomic and Molecular Physics), KOS, Greece.
Harris, R. A., 1963, *J. chem. Phys.*, **39**, 978.
Heller, E. J., 1995, *J. phys. Chem.*, **99**, 2625.
Iung, C. and Leforestier, C., 1992, *J. chem. Phys.*, **97**, 2481.
Iung, C., Leforestier, C., *et al.*, 1993, *J. chem. Phys.*, **98**, 6722.
Jortner, J. and Berry, R. S., 1968, *J. chem. Phys.*, **48**, 2757.
Kasha, M., 1950, *Disc. Faraday Soc.*, **9**, 14.
Kaufmann, J. F., Coté, M. J., Smith, P. G., and McDonald, J. D., 1989, *J. chem. Phys.*, **90**, 2874.
Kawashima, H., Wefers, M. M., *et al.*, 1995, *Ann. Rev. phys. Chem.*, **46**, 627.
Kay, K. G. and Rice, S. A., 1973, *J. chem. Phys.*, **38**, 4852.
Kellman, M. E. and Xiao, L., 1990, *J. chem. Phys.*, **93**, 5821.
Kortüm, G. and Finckh, B., 1943, *Z. Physik. Chem.* B, **52**, 263.
Kosloff, D. and Kosloff, R., 1983, *J. comp. Phys.*, **52**, 35.
Kosloff, R., Rice, S. A., *et al.*, 1989, *Chem. phys.*, **139**, 201.
Krause, J. L., Whitnell, R. M., *et al.*, 1995, *Light-Packet Control of Wave-Packet Dynamics*, edited by J. Manz and L. Woste (Weihnheim: VCH Publishers).
Kuhn, B., Boyarkin, O. V., *et al.*, 1997, *Ber. Bunsenges. Phys. Chem.*, **101**, 339.
Lawrance, W. D. and Knight, A. E. W., 1985, *J. phys. Chem.*, **89**, 917.
Lee, C. Y., and Pate, B. H., 1997, *J. chem. Phys.*, **107**, 10430.
Lehmann, K. K., 1991, *J. phys. Chem.*, **95**, 7556.
Lehmann, K. K., Scoles, G., *et al.*, 1994, *Ann. Rev. phys. Chem.*, **45**, 241.
Leitner, D. M. and Wolynes, P. G., 1996a, *J. chem. Phys.*, **105**, 11226; 1996b, *Phys. Rev. Lett.*, **76**, 216; 1997, *Chem. phys. Lett.* **280**, 411.
Lichtenberg, A. J. and Lieberman, M. A., 1983, *Regular and Stochastic Motion* (New York: Springer Verlag).
Logan, D. E. and Wolynes, P. G., 1990, *J. chem. Phys.*, **93**, 4994.
Lu, D. and Hase, W., 1988, *J. phys. Chem.*, **92**, 3217.
Madsen, D., Pearman, R., *et al.*, 1997, *J. chem. Phys.*, **106**, 5874.
Marcus, R. A., 1952, *J. chem. Phys.*, **20**, 359.
Martens, C. C., 1992, *J. stat. Phys.*, **68**, 207.
Martens, C. C. and Reinhardt, W. P., 1990, *J. chem. Phys.*, **93**, 5621.
Maynard, A. T. and Wyatt, R. E., 1995, *J. chem. Phys.*, **103**, 8372.
McIlroy, A. and Nesbitt, D. J., 1989, *J. chem. Phys.*, **91**, 104.
McIlroy, A., Nesbitt, D. J., *et al.*, 1994, *J. chem. Phys.*, **100**, 2596.
Moore, R., Doany, F. E., *et al.*, 1983, *Disc. Faraday Chem. Soc.*, **75**, 331.
Muehlbach, J. and Huber, J. K., 1986, *J. chem. Phys.*, **85**, 4411.
Munn, N. S. and Clary, D. C., 1996, *J. chem. Phys.*, **105**, 5258.
Muthukumar, M. and Rice, S. A., 1978, *J. chem. Phys.*, **69**, 1619.

NAAMAN, R., LUBMAN, D. M., *et al.*, 1979, *J. chem. Phys.*, **71**, 4192.
NAUTS, A. and WYATT, R. E., 1984, *Phys. Rev.* A, **30**, 872.
NESBITT, D. J. and FIELD, R. W., 1996, *J. phys. Chem.*, **100**, 12735.
NORDHOLM, K. S. J. and RICE, S. A., 1974, *J. chem. Phys.*, **61**, 203.
OKA, T., 1967, *J. chem. Phys.*, **47**, 5410.
PARK, S. M., LU, S., *et al.*, 1991, *J. chem. Phys.*, **94**, 8622.
PARMENTER, C. S., 1983, *Disc. Faraday Chem. Soc.*, **75**, 7.
PEARMAN, R. and GRUEBELE, M., 1998a, *J. chem. Phys.*, in the press; 1998b, to be published.
PECHUKAS, P., 1982, *Chem. phys. Lett.*, **86**, 553.
PERRY, D. S., BETHARDY, G. A., *et al.*, 1995, *Ber. Bunsenges. Phys. Bhem.*, **99**, 530.
PERSCH, G., MEHDIZADEH, E., *et al.*, 1988, *Ber. Bunsenges. Phys. Chem.*, **92**, 312.
PUTTKAMER, K. V., DÜBAL, H. R., *et al.*, 1983, *Disc. Faraday Chem. Soc.*, **75**, 197.
QIU, Y. H. and BACIC, Z., 1997, *J. chem Phys.* **106**, 2158.
QUACK, M., 1983, *Faraday Disc. Chem. Soc.*, **75**, 359.
RASHEV, S., 1990, *Chem. Phys.*, **147**, 221.
REINHARDT, W. P., 1982, *J. phys. Chem.*, **86**, 2158.
SCHERER, N. F., CARLSON, R. J., *et al.*, 1991, *J. chem. Phys.*, **95**, 1487.
SCHOFIELD, S. and WOLYNES, P. G., 1993, *J. chem. Phys.*, **98**, 1123.
SHALEV, E., KLAFTER, J., *et al.*, 1992, *Physica* A, **191**, 186.
SMALLEY, R. E., 1982, *J. phys. Chem.*, **86**, 3504.
SMITH, P. G. and MCDONALD, J. D., 1992, *J. chem. Phys.*, **96**, 7344.
STECHEL, E. B. and HELLER, E. J., 1984, *Ann. Rev. phys. Chem.*, **35**, 563.
STEPHENSON, J. C. and KING, D. S., 1978, *J. chem. Phys.*, **69**, 1485.
STEWART, G. M. and MCDONALD, J. D., 1983, *J. chem. Phys.*, **78**, 3907.
STUCHEBRUKHOV, A. A., KUZMIN, M. V., BAGRATASHVILI, V. N., and LETOKHOV, V. S., 1986, *Chem. Phys.*, **107**, 429.
STUCHEBRUKHOV, A. A. and MARCUS, R. A., 1993, *J. chem. Phys.*, **98**, 6044.
STUCHEBRUKHOV, A. A., MEHTA, A., *et al.*, 1993, *J. phys. Chem.*, **97**, 12491.
TAL-EZER, H. and KOSLOFF, R., 1984, *J. chem. Phys.*, **81**, 3967.
TRENTWITH, A. B., RABINOVITCH, B. S., *et al.*, 1982, *J. chem. Phys.*, **76**, 1586.
UZER, T., 1991, *Phys. Rep.*, **199**, 73.
WARREN, W. S., RABITZ, H. S., *et al.*, 1993, *Science*, **259**, 1581.
WU, G., 1995, *Chem. phys. Lett.*, **242**, 333; *Chem. phys. Lett.*, **248**, 77.
WYATT, R. E., 1989, *Adv. chem. Phys.*, **73**, 231; 1995, *Phys. Rev.* E, **51**, 3643.
WYATT, R. E., IUNG, C., *et al.*, 1992, *J. chem. Phys.*, **97**, 3477.
ZEWAIL, A. H., 1983, *Disc. Faraday Chem. Soc.*, **75**, 315; 1985, *Ber. Bunsenges. Phys. Chem.*, **89**, 264.
ZHANG, Y. and MARCUS, R. A., 1992, *J. chem. Phys.*, **96**, 6065.